

Paleoceanography and Paleoclimatology

RESEARCH ARTICLE

10.1029/2020PA004059

Special Section:

The Miocene: The Future of the Past

Key Points:

- The middle Miocene record of Site U1318 reveals mean annual SSTs $\sim 10^{\circ}\text{C}$ warmer than at present and registers 11 coolings
- Several of these cooling events are associated with increases in sea surface productivity (SSP)
- SSP and carbon burial on continental shelves may be key to explain the disruptions in the global carbon cycle during the middle Miocene

Supporting Information:

Supporting Information may be found in the online version of this article.

Correspondence to:

F. Sangiorgi,
f.sangiorgi@uu.nl

Citation:

Sangiorgi, F., Quaijtaal, W., Donders, T. H., Schouten, S., & Louwye, S. (2021). Middle Miocene temperature and productivity evolution at a Northeast Atlantic shelf site (IODP U1318, Porcupine Basin): Global and regional changes. *Paleoceanography and Paleoclimatology*, 36, e2020PA004059. <https://doi.org/10.1029/2020PA004059>




Received 17 JUL 2020

Accepted 1 JUN 2021

© 2021. The Authors.

This is an open access article under the terms of the [Creative Commons Attribution](https://creativecommons.org/licenses/by/4.0/) License, which permits use, distribution and reproduction in any medium, provided the original work is properly cited.

Middle Miocene Temperature and Productivity Evolution at a Northeast Atlantic Shelf Site (IODP U1318, Porcupine Basin): Global and Regional Changes

Francesca Sangiorgi¹ , Willemijn Quaijtaal² , Timme H. Donders³ , Stefan Schouten^{1,4}, and Stephen Louwye² 

¹Department of Earth Sciences, Utrecht University, Utrecht, The Netherlands, ²Paleontology and Paleoenvironment, Department of Geology, Ghent University, Ghent, Belgium, ³Department of Physical Geography, Utrecht University, Utrecht, The Netherlands, ⁴Department of Marine Microbiology and Biogeochemistry, Royal Netherlands Institute for Sea Research, Den Burg, Texel, The Netherlands

Abstract We present a high-resolution multiproxy middle Miocene sea surface temperature (SST) and productivity (SSP) reconstruction of Integrated Ocean Drilling Program Site U1318, from the upper slope edge (~ 400 m water depth) of the Porcupine Basin continental margin, eastern North Atlantic Ocean. Biomarker and dinoflagellate cyst proxies reveal warm and mostly stratified waters during the Miocene Climatic Optimum (MCO) that cooled $\sim 3^{\circ}\text{C}$ across the Miocene Climate Transition (MCT). The organic biomarker (TEX_{86} and $\text{U}^{\text{K}'}_{37}$) paleothermometers document a series of 11 transient cooling events (CEs), superimposed on the long-term climate evolution. These CEs are associated with increases in cold-water dinocysts and correlate to global benthic $\delta^{18}\text{O}$ shifts, including the Mi-2, Mi-3, and Mi-4 events. Most CEs are also associated with increases in primary productivity. A prolonged interval of high SSP between ~ 13.8 and 13.6 Ma supports the idea that carbon production (and burial) in shallow areas represents a feedback mechanism contributing to long-term atmospheric CO_2 decline and cooling during the MCT. SST comparison in three North Atlantic sites (Azores Site 608, Porcupine Basin Site U1318, and Rockall Plateau Site 982) reveals that MCO SSTs are much warmer at Site 608 than at the other two sites. The low-resolution SST record of Site 982 shows no decrease in temperature around the MCT. This may be linked to contemporaneous tectonic changes in the Tethys, Central American, and Arctic Seaways impacting local ocean circulation, superimposed on global drivers of climate change.

1. Introduction

The climate dynamics of the Miocene epoch (23.03–5.33 million years, Ma) have gained increasing attention for their potential to improve our understanding of climate sensitivity to CO_2 forcing and projected near future climate (e.g., Goldner et al., 2014; IPCC, 2014). Benthic oxygen isotope compilations indicate a global climate warmer than today (De Vleeschouwer et al., 2017; Zachos et al., 2008) at CO_2 concentrations varying from preindustrial to higher than at present. The most prominent features of the Miocene climate are a period of global warmth (Miocene Climatic Optimum, MCO, ~ 17 – 14.5 Ma) and several cold intervals, known as Mi-events (Miller et al., 1991), which represent decreasing deepwater temperatures and/or cryosphere expansion associated with sea level variations of tens of meters (John et al., 2011; Levy et al., 2019; Miller et al., 2020; Shevenell et al., 2004, 2008). Significant perturbations in the carbon cycle and biotic turnovers (e.g., Böhme, 2003; Crampton et al., 2016; Holbourn et al., 2015; Pound et al., 2012) also occurred during the Miocene, making this time period worth studying.

The MCO onset is identified by a 1‰ positive shift in the benthic foraminiferal oxygen isotope ($\delta^{18}\text{O}$) record at ~ 17 Ma, suggestive of an increase in deepwater temperature and/or a decrease in global ice volume (e.g., Holbourn et al., 2007, 2015; Lear et al., 2010, 2015). The MCO world was 7°C – 8°C warmer than present day (e.g., Herold et al., 2012; Pound et al., 2012; Steinthorsdottir, Coxall, et al., 2021; You et al., 2009), with atmospheric CO_2 concentrations of ~ 500 – 600 parts per million (ppm) (e.g., Badger et al., 2013; Foster et al., 2012; Greenop et al., 2014; Kürschner et al., 2008; Steinthorsdottir, Jardine, et al., 2021; Y. G. Zhang et al., 2013), or possibly higher (Sosdian et al., 2018, 2020). Values of ~ 500 – 600 ppm would be similar to those expected for the end of the 21st century given unabated carbon emissions (IPCC, 2014). For this reason, the MCO has been considered a possible analog for near future climate although oceanic gateway configuration was

different from that of today (e.g., Hamon et al., 2013; Jakobsson et al., 2007). High-latitude surface water temperatures during the MCO in both hemispheres were exceptionally warm, $>10^{\circ}\text{C}$ warmer than today (Levy et al., 2016; Sangiorgi et al., 2008, 2018; Schreck et al., 2013; Super et al., 2018; Warny et al., 2009). Models still fail to represent data-derived temperature gradients solely with an increase in CO_2 , as complex feedback mechanisms may have been in place (e.g., Gasson et al., 2016; Goldner et al., 2014). Local factors and changes in oceanography (e.g., sea-ice coverage and albedo, poleward ocean heat transport due to shifts in atmospheric and ocean circulation) can offer additional explanation for the sustained warmth at high latitudes (e.g., Bijl et al., 2018; Sangiorgi et al., 2018; Stuecker et al., 2018). High-resolution surface water temperature data for the MCO are needed to improve data-model comparison. The global warming during the MCO has been associated with the rapid eruption of the Columbia River Basalt Group, the strongest phase (95%) of which occurred between 16.7 and 15.9 Ma (Kasbohm & Schoene, 2018). The release of CO_2 into the atmosphere is suggested to have triggered changes in ocean carbon chemistry (Sosdian et al., 2018, 2020). Partly overlapping with the MCO, a ~ 3 Myr (~ 16.8 – 13.5 Ma) positive excursion ($\sim 1\%$) in the benthic foraminifera carbon isotope ratios ($\delta^{13}\text{C}$), known as the Monterey Carbon Isotopic Excursion (Vincent & Berger, 1985), indicates a perturbation in the carbon cycle and marine organic carbon burial. The Monterey excursion is composed of six carbon isotope maxima (CM) thought to represent carbon cycle feedback processes associated with marine productivity (Holbourn et al., 2007; Sosdian et al., 2020; Woodruff & Savin, 1991).

The end of the MCO, the Miocene Climate Transition (MCT), is a global cooling event (CE) (Mi-3) centered on 13.8 Ma. This event is contemporaneous with the most pronounced of the carbon isotope maxima (CM6), which resulted in an overall decrease in the carbon isotopic composition of the ocean (Holbourn et al., 2005, 2007; Lear et al., 2010). During the MCT, Antarctic ice sheet expanded (Holbourn et al., 2014; Lear et al., 2010; Shevenell et al., 2004), temperature decreased in both terrestrial and marine realms (Eronen et al., 2012; Flower & Kennett, 1994; Pound et al., 2012), which, together with aridification of Northern Hemisphere and midlatitudes, led to species turnover in both terrestrial and marine biota (e.g., Brennan & Keogh, 2018; Donders et al., 2009; Utescher et al., 2012). Among the most mentioned causes of the MCT are atmospheric CO_2 drawdown due to weathering (Raymo, 1991; Wan et al., 2009) or increased organic carbon burial (e.g., Flower & Kennett, 1993; Holbourn et al., 2007; Vincent & Berger, 1985; Woodruff & Savin, 1991), either marine or terrestrial (Diester-Haass et al., 2009; Kender et al., 2009). Elevated marine productivity and carbon burial on continental shelves may act as negative feedback removing CO_2 from the atmosphere (Holbourn et al., 2015; Sosdian et al., 2020; Vincent & Berger, 1985), but productivity records from continental shelves are missing. Paleoceanographic reorganization due to ocean gateway changes may have provided an alternative or additional mechanism (e.g., Hamon et al., 2013; Jakobsson et al., 2007; Shevenell et al., 2004; Woodruff & Savin, 1991; Wright et al., 1992; Y. G. Zhang et al., 2011).

Given the lack of high-resolution surface temperature data for the middle Miocene and the importance of shelf regions in regulating the carbon cycle via marine productivity, we reconstruct sea surface temperature (SST), sea surface productivity (SSP), and oceanographic changes across the MCO and the MCT at an upper slope site (water depth ~ 400 m) of the eastern North Atlantic Ocean (IODP Site U1318, Porcupine Basin, offshore Ireland, Expedition 307 Scientists, 2006) with independent multiproxy records. The aim is to investigate regional surface water changes and detect whether they correspond to proposed mechanisms and causes for global climate and carbon cycle variations. Furthermore, we present a North Atlantic perspective by comparing our SST data with the few other available data obtained from North Atlantic deep-ocean sites (DSDP 608, Azores, and ODP 982, Super et al., 2018, 2020). The analyses of Miocene climate records from different locations in the North Atlantic may help us understand the role of regional variability, superimposed on the global trends and drivers of climate change.

1.1. Site Location and Oceanography

Site U1318 (3 Holes, $51^{\circ}26.16'\text{N}$, $11^{\circ}33.0'\text{W}$; 409 m water depth; Expedition 307 Scientists, 2006) was drilled on the upper slope edge of the continental margin in the Porcupine Seabight (Figure 1), a failed rift system that originated during the opening of the North Atlantic Ocean during the Middle to Late Jurassic. During the middle Miocene the British Isles were still connected to continental Europe and there was no connection to the North Sea through the English Channel (Gibbard & Lewin, 2003; [deeptimemaps.com](https://www.deeptimemaps.com)). The

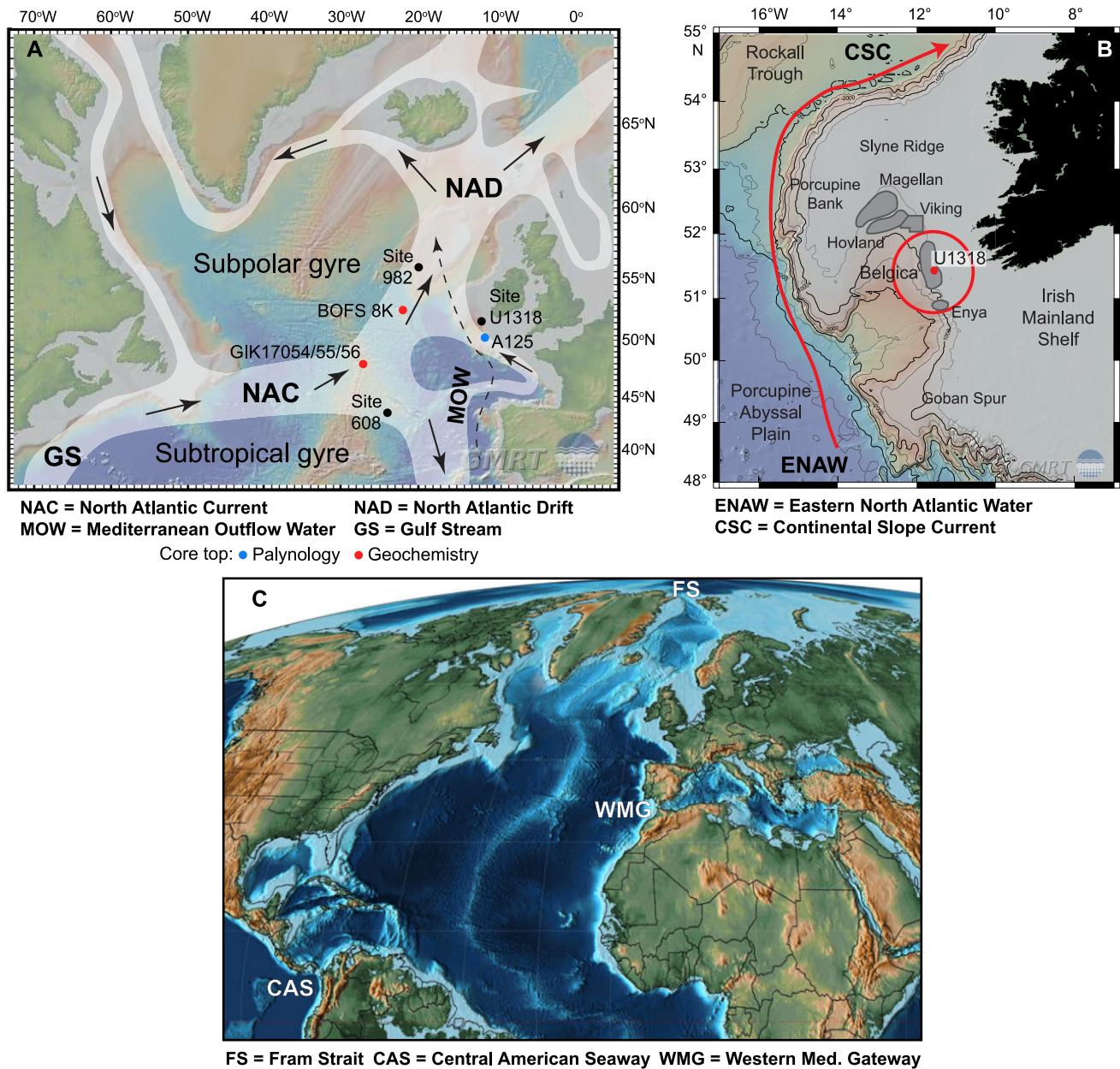


Figure 1. (a) Modern geography map of Site U1318 location (black dot), with surface currents and bathymetry (adapted from De Schepper et al. [2013]); blue dot indicates the location of the sample used for modern palynological data; red dots are modern samples where TEX_{86} and $U^{K'_{37}}$ values are available; other black dots: Miocene records used here for comparing temperature trends (Sites 982 and 608); (b) local setting of Site U1318 and the most important geographic features (coral mound provinces in gray). Red lines indicate the main surface current (ENAW, Raddatz et al., 2011). Background bathymetry created using the Global Multi-Resolution Topography (GMRT) Map tool: <http://www.marine-geo.org/tools/GMRTMapTool/>; (c) Middle Miocene (14.9 Ma) map indicating the Fram Strait (FS), the Central American Seaway (CAS), and the Tethyan (Western Mediterranean) Gateway (WMG) (modified from Scotese [2014]).

Porcupine Basin is filled with 12 km of Late Palaeozoic to Quaternary sediments (Ryan et al., 2009), mainly supplied from the Irish and Celtic shelves (Rice et al., 1991). Modern surface water temperatures (SST) at Site U1318 range between $\sim 10^{\circ}\text{C}$ in winter and $\sim 16^{\circ}\text{C}$ in summer. At a depth of 400 m, the water temperature is $\sim 11^{\circ}\text{C}$ all year round (Boyer et al., 2018, Supplemental Figure S1).

At the Porcupine bank and at Site U1318 location, the water (between 0 and 500 m depth) is composed of Continental Slope Current (CSC), which transports Eastern North Atlantic Water via the North Atlantic Current (NAC) to the Norwegian Sea (Raddatz et al., 2011, Figure 1). Subarctic Intermediate Waters, with

contribution from the Mediterranean Outflow Water, occupy the water column below (500–1,500 m), offshore the continental margin where Site U1318 is located (García-Ibáñez et al., 2015; Pollard et al., 1996). At greater depths, Labrador Sea water and Norwegian Sea Deep Water are observed (Raddatz et al., 2011). Waters are moderately productive and productivity peaks occur in spring when seasonal stratification begins and the mixed layer depth becomes shallower (Gutknecht et al., 2019; UNEP LME Report, 2008).

During the middle Miocene (~15 Ma), Site U1318 was located at a paleolatitude of ~47°N (van Hinsbergen et al., 2015) at a similar to present-day water depth (Ryan et al., 2009). Gateway configuration was different. During the early Miocene, the Fram Strait started opening and the freshwater dominated, stratified Arctic Ocean became more ventilated at ~17.5 Ma. At ~13.7 Ma, the strait deepened to present-day depth (Jakobsson et al., 2007), with implications for the Atlantic Meridional Overturning Circulation and deepwater formation (e.g., Lozier et al., 2019). Changes in lower latitude seaways (Mediterranean gateway, eastern Tethys and Central American Seaways) also occurred in the middle Miocene (~14 Ma) with important consequences for the ocean circulation reorganization and global climate. However, the exact timing of these tectonic changes is still debated (Bialik et al., 2019; Hamon et al., 2013; Montes et al., 2015; Zhang et al., 2014).

2. Material and Methods

2.1. Sediments, Age Model, and Stable Isotope Analysis

Samples were obtained from the Integrated Ocean Drilling Program (IODP) Expedition 307, Site U1318 Hole B (cores 10–14H and 17X–27X) and Hole C (cores 7H and 8X–10X, Expedition 307 Scientists, 2006; Supplemental Figure S2 and Data sets 1 and 2) between 92.4- and 247.5-m composite depth (mcd) to target the middle Miocene. The composite record was established based on physical properties (Expedition 307 Scientists, 2006). Middle Miocene sediments belong to the lithostratigraphic Unit 3 (Subunits A–C) which mainly consists of greenish-gray clay with Total Organic Carbon content (TOC%) for selected samples ranging from 0.27% to 0.70% (uppermost sample analyzed representing near modern conditions at 3.6 mbsf, TOC% = 0.25, Mangelsdorf et al., 2011) and are divided into subunits based on their calcium carbonate content (Expedition 307 Scientists, 2006; Quaijtaal et al., 2017). When material was sufficient for all analyses, 245 samples were used for oxygen and carbon stable isotopes on benthic foraminifers, palynology (dinoflagellate cysts), and organic geochemistry (U^{K}_{37} and TEX_{86}). However, some sediment samples were not sufficient for all analyses and/or were not productive. One hundred forty-five samples were analyzed for $\delta^{18}O$ and $\delta^{13}C$ on the benthic foraminifers *Uvigerina* sp. and *Cibicides pachyderma* (methodology and complete data set presented in Quaijtaal et al., 2017). Two hundred forty-five samples were analyzed for organic geochemistry and 99 samples were analyzed for palynology additional to those reported in Quaijtaal et al. (2014) (total 222).

The age model of the portion of Site U1318 record presented in this study is based on integrated bio-, isotope-, and magnetostratigraphy and is already published in Quaijtaal et al. (2017). The tie points used to build up the age model are listed in their Table 3. Samples between 92.4- and 247.5-m composite depth (mcd) cover the interval 12.75–16.60 Ma. Average time resolution for stable isotope analyses, organic geochemistry, and palynology is 25 thousands of years (kyr), 17 and 16 kyr, respectively.

2.2. Organic Geochemistry

Approximately 5 g of freeze-dried sediment was ground and extracted using accelerated solvent extraction (ASE 350 system, Dionex) using dichloromethane (DCM)/methanol (MeOH) (9:1, v/v) at 100°C and 7.6×10^6 Pa and with three static cycles for 10 min. Extracts were separated in apolar, ketone, and polar fractions over an activated Al_2O_3 column using hexane/DCM (9:1, v/v), hexane/DCM (1:1, v/v), and DCM/MeOH (1:1, v/v), respectively.

For TEX_{86} analysis, the dried polar fraction, containing tetraether lipids, was dissolved in hexane/isopropanol (99:1, v/v), filtered over a 0.45 μm polytetrafluorethylene filter (\varnothing 4 mm), and analyzed by high-performance liquid chromatography/atmospheric pressure positive ion chemical ionization mass spectrometry (HPLC/APCI-MS), following the methodology (Schouten et al., 2007). Analyses were performed on an

Agilent 1100 series LC/MSD SL and separation and a Prevail Cyano column (2.1 × 150 mm, 3 μm; Alltech), maintained at 30°C. The glycerol dialkyl glycerol tetraethers (GDGTs) were eluted isocratically using a changing mixture of hexane and propanol. The first 5 min proportions were 99% hexane:1% propanol, then increasing linearly toward 1.8% in 45 min. Flow rate was 0.2 mL/min. Single ion monitoring was set to scan the $[M + H]^+$ ions of the isoprenoid and branched GDGTs (dwell time 237 ms for each ion). TEX_{86} values were calculated after Schouten et al. (2007) and SST values were calculated following the equation: $SST_H = 68.4 \times TEX_{86H} + 38.6$, where $TEX_{86H} = \log(TEX_{86})$ (Kim et al., 2010). Analytical precision is 0.3°C based on repeated analysis of an in-house standard. Standard error on TEX_{86H} reconstructed temperatures is 2.5°C. The Bayesian calibration (BAYSPAR) (Tierney & Tingley, 2014, 2015) has also been used to calculate SST. To evaluate the reliability of the TEX_{86} and SST values, we also calculated the branched and isoprenoid tetraether (BIT) index (Hopmans et al., 2004), an indicator for continental organic matter input (Supplemental Data set 1). Following Weijers et al. (2006), we assumed that at BIT values below 0.3 TEX_{86} values were not biased by continental organic matter input. TEX_{86} can be further biased by input of GDGTs derived from methane utilizing Archaea (Y. G. Zhang et al., 2011). For this, a “Methane Index” (MI) can be calculated (Y. G. Zhang et al., 2011), which evaluates the contribution of methanotrophic archaea to the total GDGT pool (Supplemental Data set 1). MI values of 0.3–0.5 mark the boundary between “normal marine sediments” and methane-impacted sediments. Furthermore, we calculated the Ring Index (Supplemental Data set 1), which reflects archaeal communities distinct from those present at modern core top calibration sites that might indicate nontemperature effects on TEX_{86} and can be used to determine if TEX_{86} temperature estimates are influenced by nonthermal factors and/or deviate from modern analogs (Y. G. Zhang et al., 2016). Finally, we used the GDGT-2/GDGT-3 ratio as indicator of the depth of GDGT production in the water column (Taylor et al., 2013) (Supplemental Data set 1) although the water column depth is relatively shallow.

For $U_{37}^{K'}$ analysis, the ketone fraction, containing alkenones, was dissolved in hexane and injected for gas chromatography using a Hewlett Packard 6890N Network GC system equipped with a 50-m long 0.32-mm diameter silica column coated with CP Sil-5 (thickness 0.12 μm). The carrier gas used was helium. Oven temperature was programmed at 70°C for injection and increased by 20°C min⁻¹ up to 200°C, then increased by 3°C min⁻¹ until 320°C. This final temperature was maintained for 30 min. A constant pressure of 100 kPa was maintained and samples were injected on-column. Analytical precision is 0.2°C based on repeated analysis of selected fractions. Selected fractions were analyzed by GC–MS to confirm the identification of the long-chain alkenones. GC/MS was done on an Agilent 7890A GC coupled to an Agilent 5975C MS. The column, carrier gas, flow rate, and oven program were identical to the GC-FID but the end temperature was kept for 25 min. The MS operated at 70 eV, with an ion source temperature of 250°C and an interface temperature of 320°C. The injection was done on-column, with an injection volume of 1 μL. The long-chain alkenones were identified in full scan, scanning between m/z 50 and 600 and comparison with literature (de Leeuw et al., 1980; Volkman et al., 1980).

The $U_{37}^{K'}$ was calculated after Prahl and Wakeham (1987), that is, $U_{37}^{K'} = [37:2]/[37:2 + 37:3]$, SST was calculated after P. J. Müller et al. (1998): $SST = (U_{37}^{K'} - 0.044)/0.033$, global calibration (0-m water depth, 0°C–29°C modern ocean temperature). The calibration error on $U_{37}^{K'}$ reconstructed temperatures is 1.5°C (Supplemental Data set 1). The symbol ± after a value represents the standard deviation of several measurements. Instead, a ±2.5°C and a ±1.5°C indicate the standard error of calibration for TEX_{86} and $U_{37}^{K'}$, respectively.

2.3. Palynology and Palynological Indices for SST and SSP

Samples were treated with standard palynological preparation techniques. The samples were oven-dried at 60°C and ~10–15 g of dry-weight material was used, to which one or two *Lycopodium clavatum* tablets (batch no. 177745, $X = 18,584 \pm 829$ and batch no. 1031, $X = 20,848 \pm 2,186$) were added (Wood et al., 1996). Carbonates were removed using hydrochloric acid (HCl, 30%); the samples were then allowed to settle overnight and rinsed with demineralized water until pH was neutral. Samples were then processed with 40% hydrofluoric acid (HF). Fluorosilicates were removed with HCl. The residues were sieved over a 10-μm nylon mesh screen and mounted on a microscopic slide in a drop of liquid glycerol gelatin. The slides were

covered with a cover slip and sealed with nail polish. The samples are stored in the collection of the research group Paleontology and Paleoenvironment, Department of Geology, Ghent University, Belgium.

A minimum of 300 dinoflagellate cysts (dinocysts) were counted systematically, together with other palynomorphs (acritarchs, chlorophytes, organic linings of foraminifers, pollen, and spores). Slides were counted using a Zeiss AxioImagerA1 microscope at 400X magnification equipped with a Zeiss Axiocam MRc5 camera. Taxonomy follows Williams et al. (2017) and Schreck et al. (2012, 2013). Dinocyst data for the interval 12–14.3 Ma have already been published (Quaijtaal et al., 2014). Dinocyst and other palynomorph data for the entire (12.75–16.60 Ma) record are provided (Supplemental Data set 2 and Figure S3).

Dinocysts are resting stages of dinoflagellates, marine protists, with multiple trophic strategies (e.g., De Vernal & Marret, 2007; Head, 1996). The phototrophic, autotrophic dinoflagellates mostly live in the upper ~25–30 m of the water column. They are most abundant in the continental shelf, coastal to neritic environments (Pross & Brinkhuis, 2005). For the purpose of this study, that is, to provide qualitative SST and SSP reconstructions based on dinocysts, we use the ecological preferences of dinocysts as known in literature (e.g., De Schepper et al., 2009, 2011, 2013; Zonneveld et al., 2013) and calculate temperature and productivity indices as introduced in Quaijtaal et al. (2014). We selected three dinocyst species (*Nematosphaeropsis labyrinthus*, *Polysphaeridium zoharyi*, and *Operculodinium centrocarpum* sensu stricto, s.s.) for additional environmental interpretations, as their ecological niches in the modern ocean (first two species) or possible affinity to the modern species *O. centrocarpum* sensu Wall and Dale (1966) (for the third one) may aid paleoceanographic interpretations. Abundances of *N. labyrinthus*, *O. centrocarpum* s.s., and *P. zoharyi* are given with a 95% confidence interval based on the determination of a multinomial distribution for multiple taxa (following Heslop et al., 2011).

Sea Surface Temperature (SST_{DINO}). A Warm/Cold index (W/C) has often been used to evaluate changes in SST calculated as $W/C = nW/(nW + nC)$, where n is the number of specimens counted, W are warm-water indicating species, and C are cold-water indicating species (Sangiorgi et al., 2003; Versteegh, 1994). The list of warm-water species (W) and cold-water species (C) is reported in Table 2 of Quaijtaal et al. (2014). SST_{DINO} index can vary between 0 (only cold species) and 1 (warm species only). We have also calculated the concentrations (dinocysts/gram sediment) of warm and cold-water dwelling species to further support the dinocyst-based temperature reconstructions. Data are reported in Supplemental Data set 2 and Figure S3.

Sea Surface Productivity (SSP_{DINO}). A commonly used qualitative index for SSP is the P/G index (P/G; Versteegh, 1994), where $P/G = nP/(nP + nG)$, where n is the number of specimens counted belonging to the peridinioid (P) or gonyaulacoid (G) (Sangiorgi & Donders, 2004; Sluijs et al., 2005). The P/G ratio (also called H/A ratio) is based on the assumption that peridinioid species have a heterotrophic (H) feeding strategy, while most of the gonyaulacoids are phototrophs, autotrophs (A). Peridinioids feed on organic matter including phytoplankton (e.g., Jacobson & Anderson, 2008) and they usually dominate areas where high annual primary productivity is high due to high nutrients availability brought for instance by upwelling, river discharge, or high remineralization (e.g., De Vernal & Marret, 2007; Lewis et al., 1990; Pospelova et al., 2008; Sangiorgi & Donders, 2004; Zonneveld et al., 2013). The species used to represent the P group (heterotrophs) belong to the genera *Barssidinium*, *Brigantedinium*, *Cristadinium*, *Echinidinium*, *Lejeunecysta*, *Palaeocystodinium*, *Selenopemphix*, *Sumatradinium*, and *Trinovantedinium*. G group includes all other dinocysts, except the goniodomacean species (e.g., *Capisocysta* spp., *P. zoharyi*, and *Tuberculodinium vancampoeae*). SSP_{DINO} index can vary between 0 (only Gonyaulacoid phototrophic species) and 1 (only Peridinioid heterotrophic species). The higher the P/G ratio, the higher the productivity. We calculated the P-cyst concentrations (P-cysts/gram) to strengthen the productivity reconstruction. P-cysts are notably more sensitive than G-cysts to bottom water oxygenation and their % in the record (hence the P/G ratio) could be biased by changes in oxygen availability through time (e.g., Versteegh & Zonneveld, 2002) although a strong relationship between P/G and primary productivity in modern settings has been found (Pospelova et al., 2008). Evaluating P-cysts concentration next to P/G ratio provides a way to distinguish between productivity and preservation (Reichart & Brinkhuis, 2003). Data are presented in Supplemental Data set 2 and Figure S3.

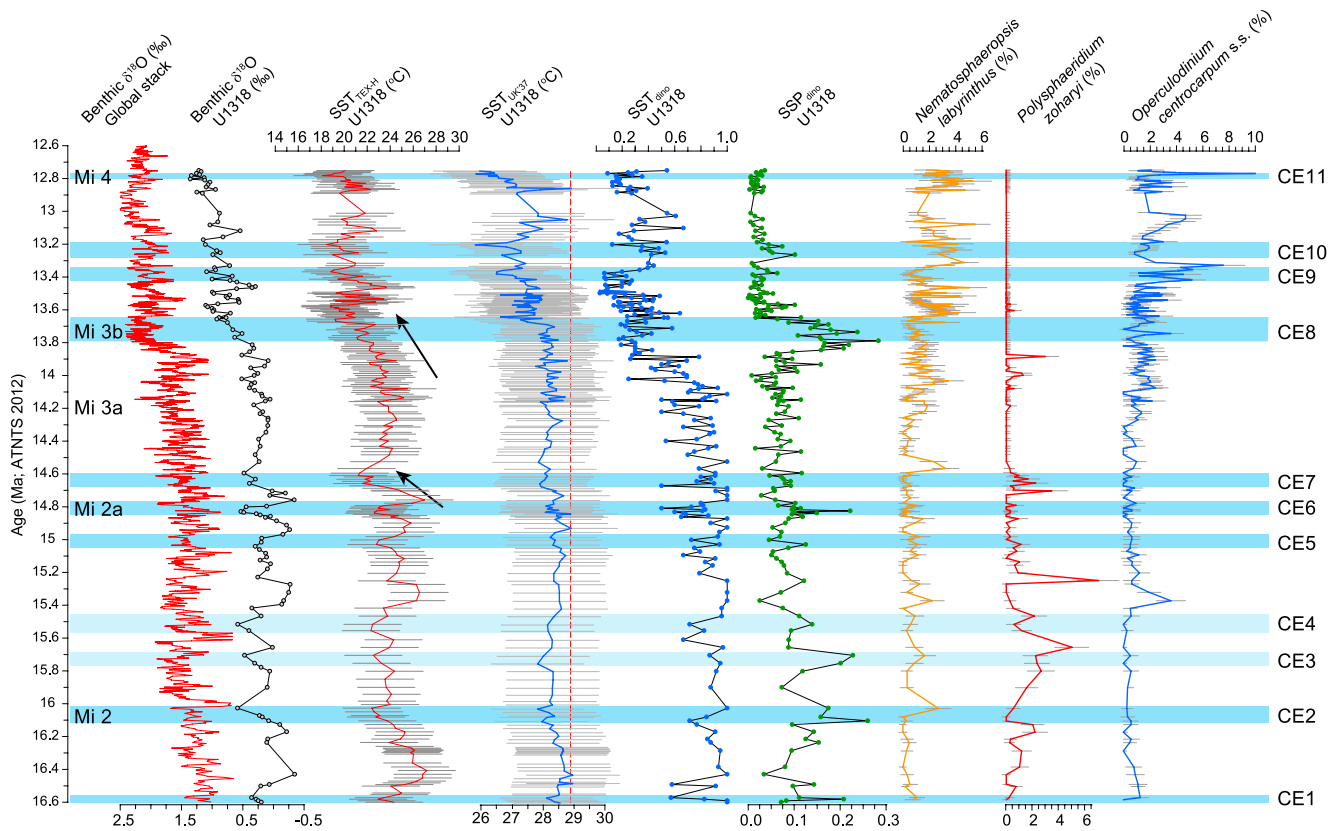


Figure 2. Middle Miocene multiproxy SST and SSP record, Site U1318. Cooling Events (CE) identified in the record are marked with blue horizontal bars (light blue = cooling events identified by <3 datapoints). Globally recognized Miocene cooling events (Mi-2, Mi-2a, Mi-3a, Mi-3, and Mi-4) are indicated. From left to right: global benthic $\delta^{18}\text{O}$ (De Vleeschouwer et al., 2017); benthic $\delta^{18}\text{O}$ at Site U1318; TEX_{86} -based SST reconstruction ($\text{SST}_{\text{TEX-H}}$) based on the Kim et al. (2010) calibration; $\text{U}^{K'_{37}}$ -based SST reconstruction (SST_{UK}) based on the P. J. Müller et al. (1998) calibration (error bars are calibration errors). Qualitative SST (SST_{DINO}) and SSP (SSP_{DINO}) based on dinoflagellate cyst assemblages; percentages of three representative dinoflagellate cyst species (*Nematosphaeropsis labyrinthus*, *Polysphaeridium zoharyi*, and *Operculodinium centrocarpum* s.s.) plotted with a 95% confidence interval based on a determination of a multinomial distribution for multiple taxa (following Heslop et al., 2011). SST, sea surface temperature; SSP, sea surface productivity.

3. Results

3.1. Sea Surface Temperature at IODP Site U1318

TEX_{86} -based sea surface temperature ($\text{SST}_{\text{TEX-H}}$) varies between $\sim 18^\circ\text{C}$ and $\sim 27^\circ\text{C}$ (Figure 2) and between $\sim 15^\circ\text{C}$ and $\sim 28^\circ\text{C}$ when using the BAYSPAR calibration ($\text{SST}_{\text{TEX-BAY}}$, Figure 3). Minimum and maximum SSTs are reached at 12.8 and 16.4 Ma, respectively, regardless of the calibration used. Indeed, the two calibrations show very similar values, although the BAYSPAR calibration generally depicts higher variability and lower SSTs after 13.9 Ma. The overall record corresponds in remarkable detail to the Site U1318 benthic oxygen isotope data published earlier (Quaijtaal et al., 2017, Figure 2).

Superimposed on a long-term $\sim 9^\circ\text{C}$ cooling, $\text{SST}_{\text{TEX-H}}$ records several transient 1.5°C – 6°C CEs, numbered here CE1–11 (Figure 2). A drop in $\text{SST}_{\text{TEX-H}}$ in multiple (≥ 3) samples is indicated with blue bars, while cooling episodes based on few (2) datapoints are marked in light blue. In the interval between 16.6 and ~ 14.7 Ma, average $\text{SST}_{\text{TEX-H}}$ ($24.5^\circ\text{C} \pm 1.3^\circ\text{C}$) values are generally higher than in the younger part of the record (average $21.6^\circ\text{C} \pm 1.7^\circ\text{C}$).

The most pronounced event, CE7, is part of a 6°C decline in $\text{SST}_{\text{TEX-H}}$ from 14.76 to 14.61 Ma. Another remarkable event is CE8, which is superimposed on a long-term cooling trend, occurs between 14.20 and 13.66 Ma and corresponds to a temperature drop of $\sim 3^\circ\text{C}$. A third pronounced cooling step (CE11) of $\sim 3^\circ\text{C}$ is recorded between 12.83 and 12.78 Ma.

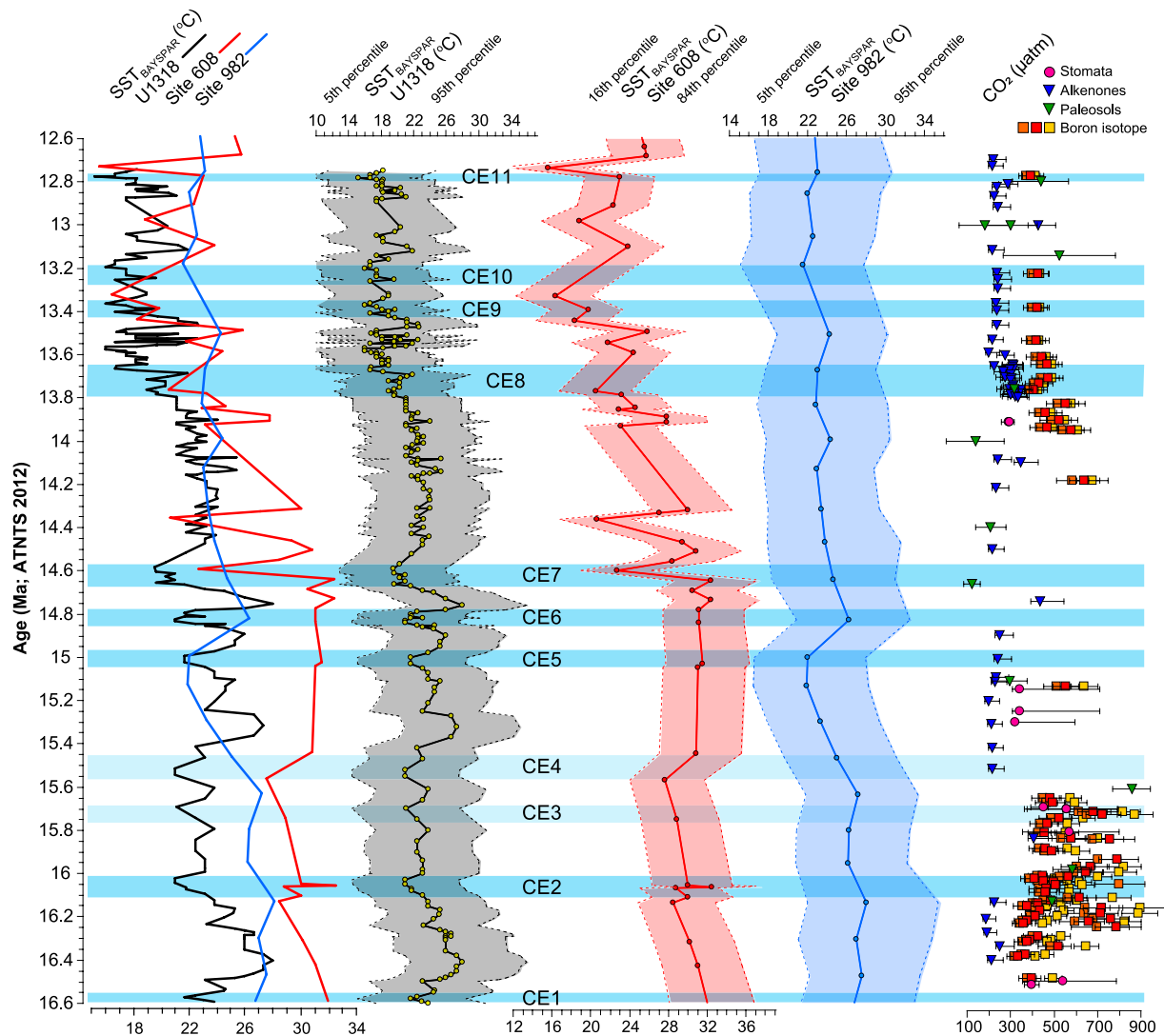


Figure 3. Comparison of SST records from DSDP Site 608 (Super et al., 2018), ODP Site 982 (Super et al., 2020), and IODP Site U1318 plotted using BAYSPAR calibration (Tierney & Tingley, 2015) for the interval 16.6–12.7 Ma. CO₂ (µatm) concentrations based on stomata (Kürschner et al., 2008), alkenones (Y. G. Zhang et al., 2013), paleosols (Retallack, 2009), and Boron isotopes (from Sosdian et al., 2018, 2020). SST, sea surface temperature.

To check for any bias in the TEX₈₆ record, we screened the data for several criteria (Supplemental Data set 1 and Figure S4). No TEX₈₆ values were discarded because of terrestrial input, as BIT was <0.1 throughout the record, which is well below the accepted threshold of 0.3 (Weijers et al., 2006). The values for the MI indicate that there is no substantial input of methanotrophic or methanogenic archaea (Y. G. Zhang et al., 2011). TEX₈₆ is primarily derived from marine Thaumarchaeota as shown by the small (<0.3) deviation in the Ring Index (Y. G. Zhang et al., 2016). The GDGT-2/GDGT-3 ratio (Taylor et al., 2013) is quite constant (1.9–3.0) implying there is no remarkable difference in the depth of GDGTs production as expected in a relatively shallow water location. In the part of the record between 15.5 and 12.7 Ma, GDGT-2/GDGT-3 ratios are generally higher (2.7 ± 0.2) than in the interval 16.6–15.6 Ma (2.2 ± 0.2), but this shift does not correspond to any remarkable changes in the SST_{TEX-H} (Figure 2). There is a weak significant correlation between GDGT-2/GDGT-3 ratios and TEX₈₆ ($R^2 = 0.31$; $p < 0.0001$, supplemental Figure S4) suggesting no major bias due to depth changes.

U^K₃₇-based SST (SST_{UK37}) is on average 3°C–8°C higher than the SST_{TEX-H}, with temperatures between 25.8°C and 29.0°C (Figure 2 and Supplemental Data set 2). SST_{UK37} trends resemble that of SST_{TEX-H} and

show a major cooling step at ~ 13.64 Ma (min $SST_{UK37} = 26.6^{\circ}\text{C}$), which separates an interval with low ($\sim 1^{\circ}\text{C}$) SST_{UK37} variability (16.60–13.64 Ma) from one with higher SST_{UK} variability (up to 3°C at 13.2 Ma, between 13.64 and 12.7 Ma).

SST relative changes, as calculated with the index based on dinocyst (SST_{DINO}) assemblages and warm dinocyst concentrations (Supplemental Figure S3), show prevailing warm waters between 16.60 and 14.04 Ma, followed by a gradual cooling, a major cooling step at 13.88 Ma, and others at 13.53 and 12.85 Ma. The cold-water dinocyst concentrations are always higher than those of warm dinocysts in younger part of the record (13.88–12.75 Ma). Considering the species responsible for the CEs, the CEs 1–7 are caused by a decrease in warm-water species and a sudden appearance of cold-water indicators *Bitectatodinium tepikiense* and *Impagidinium pallidum*, although in low abundances (Supplemental Data set 2 and Figure S3). In the modern ocean, these species are associated with (sub)polar cold, well-ventilated nutrient-rich waters. However, *I. pallidum* has also been found in high abundances at SST s as high as 10°C – 15°C in the Pliocene and Miocene of the North Atlantic and in low abundances even at higher temperatures (De Schepper et al., 2011; Schreck et al., 2017). The younger CEs (CEs 8–11) are instead mostly caused by peaks (up to 35% of the assemblage) of *Habibacysta tectata* and lower abundances of *Filispheera filifera*, both extinct species. *Habibacysta tectata* abundances similar to those found in our record have been associated to SST of $\sim 15^{\circ}\text{C}$ – 20°C in other Pliocene and Miocene records (De Schepper et al., 2011; Schreck et al., 2017). The temperature information obtained from dinocysts is comparable to that derived from SST_{TEX-H} ; during CEs mean annual temperature rarely dropped below 15°C .

SST_{DINO} mirrors both the long-term cooling trend as well as the transient SST decreases present in the SST_{TEX-H} and the benthic $\delta^{18}\text{O}$ increases (Figure 2, Quaijtaal et al., 2014).

3.2. Sea Surface Productivity and Oceanographic Conditions at Site U1318

The Peridinioid/Gonyaulacoid (P/G) ratio based on dinocysts varies between 0 and 0.3 (Figure 2, Supplemental Data set 2 and Figure S3). Compared to the average value of 0.07, the highest values (>0.2) in the P/G ratio occur at 16.58, 16.10, 15.71, 14.83 Ma, and between 13.84 and 13.57 Ma and at 13.26 Ma. Increases in P/G ratio are supported by peaks in P-cyst concentrations (Supplemental Figure S3), particularly high at 15.70 Ma ($\sim 3,600$ cysts/g), 14.8 Ma ($\sim 6,600$ cysts/g), and between 13.84 and 13.57 Ma (4,000–8,300 cysts/g).

To further constrain interpretation of paleoenvironments, the ecological preferences of three dinocysts species are considered (Figure 2). It is worth mentioning that the dinocyst assemblages in the Miocene record of Site U1318 are dominated by *Spiniferites/Achomosphaera* complex, indicating the proximity to the shelf (e.g., Zonneveld et al., 2013; Supplemental Figure S3). *Nematosphaeropsis labyrinthus*, a species abundant in the modern ocean frontal systems, is present in percentages generally lower than 2% between 16.6 and 13.61 Ma and significantly increases to values up to 6% after 13.61 Ma. *Polysphaeridium zoharyi* prefers warm and stratified waters. Here, it is almost constantly present between 16.6 and 14.6 Ma and virtually absent after 13.9 Ma. *Operculodinium centrocarpum* s.s. is never very abundant, but its percentages tend to increase from about 13.8 Ma and reaches its highest value (11%) at the top of the record (12.7 Ma). If we assume that *O. centrocarpum* s.s. shares the same ecological niche with the extant species *O. centrocarpum* sensu Wall and Dale (1966), it represents a cosmopolitan species, well adapted to unstable conditions, and found where oceanic and neritic waters mix at continental margins (e.g., Dale, 1996). In the North Atlantic, high abundances of *O. centrocarpum* sensu Wall and Dale (1966) reflect the influence of the NAC (De Schepper et al., 2011; Hennissen et al., 2014).

4. Discussion

4.1. Comparison Among Different Temperature Proxies

The best and most striking correlation between temperature proxies is found between SST_{TEX-H} and benthic $\delta^{18}\text{O}$ records ($R^2 = 0.88$; $p < 0.0001$) (supplemental Figure S5). The correlations between SST_{TEX-H} and SST_{UK37} ($R^2 = 0.66$; $p < 0.0001$), SST_{TEX-H} and SST_{DINO} ($R^2 = 0.54$; $p < 0.0001$), and SST_{UK37} and SST_{DINO} ($R^2 = 0.42$, $p < 0.0001$) are lower but still significant. These correlations suggest that there is likely one dominant controlling factor on these individual proxies, that is, temperature, although other factors might

contribute to the lower degree of correlation between some proxies (e.g., seasonality, water column depth, biases related to ammonium oxidation rates on TEX_{86} , maximum temperature limit of $U^{K'}_{37}$ [$\sim 29^\circ\text{C}$], ice volume component on benthic oxygen isotope records).

At present, CSC, ENAW waters occupy the entire water column at Site U1318 (51.5 N; 11.5 W, Figure 1). Measured mean annual SST is 12.6°C , 10.5°C in winter and 15.6°C in summer when a thermocline develops in the upper (~ 30 m) layer as consequence of atmospheric warming (Boyer et al., 2018, Supplemental Figure S1).

We tested the paleothermometry proxies on modern surface sediment samples. Unfortunately, the only nearby surface sediments where $U^{K'}_{37}$ and TEX_{86} have been measured are in a deepwater location to the west of Site U1318, under the influence of NAC (Figure 1). $\text{SST}_{\text{TEX-H}}$ measured in sample BOFS8K ($\sim 52.5^\circ\text{N}$, 22°W , $\sim 4,000$ m water depth, at present ~ 700 km to the west of Site U1318) where mean annual SST is 12°C (Boyer et al., 2018) returns a value of $15^\circ\text{C} \pm 2.5^\circ\text{C}$ ($\text{TEX}_{86} = 0.45$, Kim et al., 2010), indicating that $\text{SST}_{\text{TEX-H}}$ may represent mean annual temperature. Samples GIK17054/55/56 (three samples around 48.5°N , 26°W , $\sim 2,000$ – $3,000$ m water depth, Figure 1, at present $\sim 1,000$ km to the west of Site U1318) yield $U^{K'}_{37}$ values of 0.54, 0.57, 0.59, respectively (P. J. Müller et al., 1998; Rosell-Melé et al., 1995), which fall well within the calibration line of $U^{K'}_{37}$ versus annual mean SST, suggesting that in the present setting $U^{K'}_{37}$ may represent mean annual SST.

In our Miocene record, $\text{SST}_{\text{TEX-H}}$ is several degrees (average $10.0^\circ\text{C} \pm 2.1^\circ\text{C}$) higher than modern mean annual SST at Site U1318, while SST_{UK} temperatures are on average $15.3^\circ\text{C} \pm 0.6^\circ\text{C}$ higher than modern mean annual SST. One explanation for such difference between the two lipid-based paleothermometers could be the different growth seasons of the organisms on which the temperature proxies are based. Coccolithophorids, the organisms producing alkenones (SST_{UK}), usually bloom in spring and summer (April–July) in the North Atlantic (e.g., Shutler et al., 2013), while the Thaumarchaeota ($\text{SST}_{\text{TEX-H}}$) can be abundant all year round, even in winter (Bale et al., 2013; O. Müller et al., 2018; Pitcher et al., 2011). Alternatively, $\text{SST}_{\text{TEX-H}}$ may represent a deeper than surface water signal (e.g., Besseling et al., 2019; Ho & Laepple, 2016). Site U1318 is located at shallow water depth (400 m) and measured mean annual SSTs at surface and at maximum depth differ by 2.5°C (Boyer et al., 2018). Locations where high contribution of deep Thaumarchaeota may affect $\text{SST}_{\text{TEX-H}}$ as surface signal are usually upwelling systems and/or areas where the water column is $>1,000$ m depth (Taylor et al., 2013), unlike our study site. An additional cause for the offset between $\text{SST}_{\text{TEX-H}}$ and SST_{UK} may be due to the import of allochthonous material from warmer regions and/or alkenones preferential selective degradation, which has shown to produce temperature increases of up to 1.8°C (Kim et al., 2009). Several studies have shown that the TEX_{86} is less impacted by lateral transport than $U^{K'}_{37}$ as GDGTs degrade quicker than alkenones, leading to relatively higher allochthonous input for alkenones (Kim et al., 2009; Mollenhauer et al., 2008). Another potential bias could be due to archaeal ammonium oxidation rates on TEX_{86} (Hurley et al., 2016) which may have varied over the Miocene and introduce amplifications of temperature trends in TEX_{86} records and relates to productivity (Lawrence et al., 2020). Cross correlation between TEX_{86} and the dinocyst-based productivity (P/G ratio) proxy shows poor ($R^2 = 0.24$; $p < 0.0001$) correlation. It should also be noted that $U^{K'}_{37}$ index is well above the value 0.9 in all samples and equal to or higher than 0.95 in 201 of the 245 samples analyzed (Supplemental Data set 1). This could imply that saturation is reached and temperatures experienced by haptophytes could have been even higher, which would explain the lower variability of the SST_{UK} compared to $\text{SST}_{\text{TEX-H}}$. If SST_{UK} represents surface water summer temperature, summer temperatures during the middle Miocene would have been $27.9^\circ\text{C} \pm 0.6^\circ\text{C}$ (average SST_{UK} in the record), $\sim 12^\circ\text{C}$ warmer than at present. Such high summer temperatures throughout the Miocene record would question the presence of cold-temperate water dinocysts, which become very abundant (up to $\sim 8,000$ dinocysts/g sediment) in the interval between 13.84 and 13.57 Ma (Quaijtaal et al., 2014, 2017, SST_{DINO} , Figure 2; Supplemental Figure S3). Dinoflagellates live in the upper ~ 30 m and are most abundant during summer in the North Atlantic (e.g., Barton et al., 2015). The production of different dinocyst species in different seasons in coastal sites has been investigated with sediment traps studies (e.g., Fujii & Matsuoka, 2005; Pospelova et al., 2018; Ribeiro & Amorim, 2008). Records usually indicate that an increase in (heterotrophic) P-cysts is mostly dependent on prey (e.g., diatoms) availability and usually occurs in autumn (or winter). Autotrophic (phototrophic) G-cyst species depend directly on local physical and chemical environment factors, and cyst production occurs throughout the year.

Rather than a clear seasonal pattern, interannual variability is more important (Ribeiro & Amorim, 2008). We included 20 different species in the SST_{DINO}. We are hence confident that a strong seasonal bias due to seasonal production of temperature related dinocyst species can be excluded. Although qualitative, SST_{DINO} (supported by the concentration of cold-water loving species, Supplemental Figure S3) indicates shifts toward colder water conditions in several parts of the record.

Given the above, we speculate that SST_{TEX-H} values may be more indicative than SST_{UK} of mean annual temperature changes though we cannot exclude complications due to changes in archaeal ammonium oxidation rates.

The benthic foraminiferal $\delta^{18}\text{O}$ (Figure 2) at Site U1318 shows good similarity with the benthic foraminiferal $\delta^{18}\text{O}$ stack (De Vleeschouwer et al., 2017) but has also clear differences. The different resolution between the two records makes a direct comparison difficult. The major trends are similar, the $\delta^{18}\text{O}$ values are lower (as expected at a shallower site) but variability is similar (average $0.46\text{‰} \pm 0.72\text{‰}$ compared to $1.58\text{‰} \pm 0.71\text{‰}$, in De Vleeschouwer et al., 2017). The strong correlation between SST_{TEX-H} and benthic foraminiferal $\delta^{18}\text{O}$ may suggest that SST_{TEX-H} includes a deeper component and reflects subsurface water signal. At present, the difference between mean annual temperature at the surface (0 m, 12.6°C) and at the seafloor (400 m, 10.7°C) is low ($\sim 2^\circ\text{C}$), and the water below 100 m has virtually the same temperature all year round. The calibration uncertainty of the TEX₈₆-based SST proxy is $\pm 2.5^\circ\text{C}$, which precludes distinguishing between surface and subsurface signal. Furthermore, we note that most studies indicate that TEX₈₆ in surface sediments is generated predominantly in the upper waters (100–200 m) and not in the sediment itself (e.g., Lengger et al., 2013). Given that the SST_{TEX-H} from the modern sediment sample best reflects surface and not bottom water temperatures, SST_{TEX-H} at this site is likely to represent temperature of the upper waters.

Most of the CEs recorded at Site U1318 in both the SST_{TEX-H} and benthic foraminiferal $\delta^{18}\text{O}$ data are accompanied by SST_{DINO} shifts toward lower values, suggesting cooling of the entire water column, with SST_{DINO} representing surface conditions, SST_{TEX-H} (sub)surface conditions and benthic $\delta^{18}\text{O}$ bottom water (400 m depth) conditions. SST_{UK} may be mostly indicative of summer conditions.

4.2. Productivity and Oceanographic Changes at Site U1318

The majority of the CEs are accompanied by an increase in productivity (SSP_{DINO} and P-cysts concentrations, Figure 2, Supplemental Figure S3). This correspondence is particularly clear for events CE1, CE2, CE3, CE6, and CE8, suggesting that cooling and an increase in nutrients in the upper water column were related. Nutrient-rich surface waters can be the result of more vigorous mixing of the water column, upwelling, changes in ocean currents, proximity to land during global cooling, and sea level drop and consequent displacement of shelf material, or river input. At present, dinocyst assemblage from a site close to Site U1318 (A125, Zonneveld et al., 2013, $\sim 50.3^\circ\text{N}$, 11.6°W , Figure 1) is composed of 1% Peridinioid cysts only (SSP_{DINO} = 0.01, Supplemental Figure S1). SSP_{DINO} values as high as 0.2–0.3 (compared to average 0.07 of the entire Miocene record) and increases in P-cysts concentrations (Supplemental Figure S3 and Data set 2) demonstrate that primary productivity was on average higher than at present and increased significantly during some of the cold events (Figure 2), in particular between 13.84 and 13.57 Ma. We correlated SSP_{DINO} and BIT to test whether higher terrestrial organic matter input (e.g., via river input) could have caused the increase in productivity. The explained variation is very low ($R^2 = 0.09$; $p < 0.0001$, supplemental Figure S5), dismissing this cause. Moreover, the few pollen present in the record (Supplemental Figure S3) are also indicative of moderate to low terrestrial input and certainly negligible after 15.5 Ma. The lithology of the core does not show major changes (clay to fine sand), and the observed increases in fine grain sand particles ($>63\ \mu\text{m}$) do not correspond to peaks in productivity (Supplemental Figure S2). This is particularly true for the highest productivity peak between 13.84 and 13.57 Ma. At present, SSP_{DINO} (P/G ratio) values of ~ 0.2 – 0.3 in shelf areas are found in the North Adriatic Sea (Sangiorgi & Donders, 2004), Northern Gulf of Mexico (Limoges et al., 2014) both offshore a river plume, and in the Northern Jorge Gulf (Patagonia) where waters from offshore well up on the shelf (Faye et al., 2018). Excluding the influence of nutrient-rich riverine waters as cause for increased productivity, and in absence of a relationship between productivity and sediment grain size or pollen/spores (Supplemental Figures S2 and S3), which could point to a coastline closer to the site and higher displacement of material from the shore, we submit that increased mixing

of the water column during cold intervals provided the nutrients to sustain productivity in the surface waters. Rearrangements in the Tethys Seaways at ~14 Ma initiated the Mediterranean Outflow Water, a water mass flowing through the western Mediterranean Gateway into the Atlantic Ocean (MOW, Figure 1, Bialik et al., 2019). At present, MOW is a high salinity, nutrient-rich water mass (Coste et al., 1988; Huertas et al., 2012) that occupies the water column below 500 m depth to the west of drill site. Whether this water mass could have influenced the nutrient content of the surface waters at Site U1318 around ~13.8 Ma is unknown.

Modern dinocyst assemblage at A125 is dominated by *O. centrocarpum* (89%), followed by *Spiniferites* spp. (4%), *N. labyrinthus* (3%), and *P. zoharyi* is absent. *Polysphaeridium zoharyi* is the cyst of a red tide forming, potentially toxic dinoflagellate, *Pyrodinium bahamense* (e.g., Usup et al., 2011). It thrives in warm (summer temperatures up to 29°C), saline (seasonally) stratified water environments, and is never observed north of 30°N (Zonneveld et al., 2013). *Polysphaeridium zoharyi*'s near-continuous presence at Site U1318 between 16.6 and 14.6 Ma confirms that waters must have been much warmer and more stratified than today's during the MCO. Interestingly, when *P. zoharyi* is present, it generally decreases in abundance when productivity increases (Figure 2). This could confirm that more vigorous water mixing during cooling episodes sustained productivity. Its disappearance after ~13.8 Ma is in line with the average ~3°C SST cooling recorded by SST_{TEX-H} during the MCT, while SST_{UK} is still high (~28°C). In our Miocene record, the highest (3.5%–10%) percentages of *O. centrocarpum* s.s. occur in the record between ~13.75 and 12.75 Ma. If its ecological affinity is similar to that of the extant *O. centrocarpum*, significantly higher percentages (exceeding the confidence interval) may indicate environmental conditions became generally more unstable. Interestingly, the age of ~13.7 Ma coincides with that of the MCT and that of a fully ventilated Arctic Ocean following complete opening and deepening of the Fram Strait (Jakobsson et al., 2007; Sangiorgi et al., 2008). Other major tectonic rearrangements (Tethys and Central American Seaways) seem to have occurred around 14 Ma (Bialik et al., 2019; Montes et al., 2015; Zhang et al., 2014). Simultaneous changes in the oceanography at Site U1318 are also recorded by a small, but significant increase in *N. labyrinthus*, which best thrives in proximity of frontal systems, when waters with different temperature come into contact (Boessenkool et al., 2001; Prebble et al., 2013).

In general, the dinocyst assemblages of the entire middle Miocene record remain different from the modern ones but show clear changes at ~13.8 Ma.

4.3. Cooling Events at Site U1318: Regional Versus Global

The majority of the surface CEs (CE, Figure 2) at Site U1318 are mirrored by increases in global benthic $\delta^{18}\text{O}$ record (De Vleeschouwer et al., 2017), including Mi-2 (~16 Ma, CE2), Mi-2a (~14.8 Ma, CE6/CE7), Mi-3 (~13.8 Ma, CE8), and Mi-4 (~12.8 Ma, CE11). We will now focus the discussion on relating these global events to regional climate and oceanography changes. All the other CEs are considered regional changes, with minor expression in the global $\delta^{18}\text{O}$ record.

The first, transient cooling (CE2, 16.03 Ma, Figures 2 and 3) can be correlated to Mi-2. A first cooling step in SST_{DINO} and an increase in productivity (SSP_{DINO}, P-cyst concentration, Supplemental Figure S3) occur at the beginning of a 0.93‰ benthic $\delta^{18}\text{O}$ excursion at Site U1318, accompanied by a ~3°C SST_{TEX-H} (~0.3°C SST_{UK}) cooling. During the maximum temperature drop, reduced stratification (decrease in *P. zoharyi*) and waters masses with contrasting characteristics (*N. labyrinthus* peak) are present. The benthic $\delta^{18}\text{O}$ global record change in the same time interval is 0.43‰, about half of the signal recorded at Site U1318. Using backstripping solutions and benthic $\delta^{18}\text{O}$ and Mg/Ca records, eustatic sea level is estimated to have dropped ~30–40 m during Mi-2 (John et al., 2011; Miller et al., 2020), under atmospheric CO₂ concentrations (~400–600 ppmV, Sostdian et al., 2020, Figure 3) clearly lower in absolute values and range compared to the intervals before and after. Productivity is relatively high during the entire interval.

The second marked cooling phase (CE5, CE6, and CE7, 15.05, 14.84, and 14.61 Ma, respectively Figure 2), is a ~400 kyr interval centered on the age of Mi-2a (14.8 Ma, Miller et al., 2020). CE5 is mainly detectable in SST_{TEX-H} and corresponds to a small rise in productivity, while changes in SST_{UK}, benthic foraminifer $\delta^{18}\text{O}$ and SST_{DINO} are less evident. Instead, CE6 represents a significant ~2–3°C SST_{TEX-H} (~1°C SST_{UK}) decrease coeval with a positive $\delta^{18}\text{O}$ excursion of 0.5‰ (Figure 2). Similarly to CE2, CE6 is identified by a sharp initial

decrease in SST_{DINO} and a prominent but temporary increase in productivity, while *P. zoharyi* indicates a general decrease in warmth and water column stratification. Surface cooling and productivity correspond to a maximum global deepwater cooling ($\sim 1\%$ increase in global benthic $\delta^{18}\text{O}$ record change, De Vleeschouwer et al., 2017) associated with Mi-2a. Mi-2a has been linked to an eustatic sea level fall of ~ 30 m and a cooling of $\sim 0.7^\circ\text{C}$ in deep waters (John et al., 2011; Miller et al., 2020). CO₂ concentration values are extremely sparse and seem to point to values generally lower than 300 ppmV (Figure 3).

During CE7, a sharp decrease in SST_{DINO} marks the beginning of a long gradual SST_{TEX-H} cooling of $\sim 5^\circ\text{C}$ down to 21°C (SST_{UK} decrease of $\sim 1^\circ\text{C}$ down to 28°C), accompanied by an increase in benthic $\delta^{18}\text{O}$ of 0.8% at Site U1318. A comparable $\delta^{18}\text{O}$ excursion of 0.75% is observed in the deep ocean (De Vleeschouwer et al., 2017). Productivity is constantly, but minimally, above average values, and water stratification seems to be in place (*P. zoharyi* is present). The few CO₂ reconstructions available for this interval depict a drop from ~ 400 ppm precooling (at ~ 14.7 Ma, Y. G. Zhang et al., 2013) to 116 ppm (at ~ 14.6 Ma, based on 1 measurement on paleosols, Retallack, 2009; Figure 3). Regardless of the CO₂ concentration values, the remarkable drop in SST observed at Site U1318 does not seem to be accompanied by any major changes in the oceanography, including productivity, which is only slightly above average at Site U1318.

After CE7, proxies indicate an environment with generally colder and less stratified surface waters. SST_{DINO} shows gradual cooling starting at 14.12 Ma, followed by a sharp decline while SST_{TEX-H} decreases from ~ 13.89 Ma toward the CE8 cooling at 13.8 Ma (Figure 2). The overall surface water SST_{TEX-H} temperature decrease is $\sim 5^\circ\text{C}$ – 6°C Ma (SST_{UK} $\sim 2^\circ\text{C}$). The sharp SST_{DINO} decline at ~ 13.89 Ma is simultaneous with the start of a gradual positive excursion of $\sim 1\%$ in the global benthic $\delta^{18}\text{O}$ ($\delta^{18}\text{O}$ shift at Site U1318 is $\sim 0.9\%$), which corresponds to the Mi-3 event. Mi-3 is associated with cooling in the deep ocean of 1.2°C , ~ 50 m eustatic sea level fall (De Vleeschouwer et al., 2017; Miller et al., 2020), and declining atmospheric CO₂ concentrations (from ~ 600 to ~ 400 – 500 ppm, Sossdian et al., 2020, Figure 3). Dinocyst proxies (Figure 2, Supplemental Figure S3 and Data set 2) show remarkably high productivity, which lasted for a period of ~ 200 kyr. High productivity on continental margins at global scale, if accompanied by carbon burial, can certainly contribute to CO₂ withdrawal from the atmosphere and to the global cooling at the MCT. Indeed, this interval corresponds to the so-called CM6 event, one of the most pronounced CM detected in the deep ocean, which indicates a drastic change in the global carbon cycle (Holbourn et al., 2004; Lear et al., 2010; Sossdian et al., 2020).

CE11 at ~ 12.78 Ma is part of a cooling trend that started at ~ 13.12 Ma. This cooling, especially pronounced in the surface water proxies, is of a smaller magnitude than CE8 (Mi-3), both in benthic $\delta^{18}\text{O}$ (0.71%) and in SST_{TEX-H} and SST_{UK} ($\sim 3^\circ\text{C}$; Figure 2). This cooling corresponds to the Mi-4 event (~ 12.9 Ma), which has been associated with a shift in global benthic $\delta^{18}\text{O}$ of $\sim 0.5\%$, a drop in deepwater temperature of $\sim 1^\circ\text{C}$ and sea level fall of ~ 20 – 30 m (De Vleeschouwer et al., 2017; Miller et al., 2020) and mostly preindustrial atmospheric CO₂ concentrations (Figure 3). The presence of a small hiatus prior to the Mi-4 (Quaijtaal et al., 2014) has possibly prevented to capture this event fully at the Porcupine Basin. During this event, dinocysts show low productivity and *O. centrocarpum* s.s. percentages reach $\sim 10\%$.

The CEs identified in our record that correspond to known global CEs (CE2, CE6, CE8, and CE11) show an upper water temperature drop of $\sim 3^\circ\text{C}$. Both CE6 (Mi-2a) and CE8 (Mi-3) correspond to shifts in global benthic $\delta^{18}\text{O}$ of $\sim 1\%$ (De Vleeschouwer et al., 2017), while at shallow Site U1318 $\delta^{18}\text{O}$ increases are $\sim 0.5\%$ and 0.9% , respectively.

CE8 represents the peak of a SST cooling trend (6°C in total) that started ~ 14.2 Ma at Site U1318 (Figure 2) and affected the entire water column (~ 400 m deep). At a global scale, CE8 is associated with a ~ 50 m sea level drop (Miller et al., 2020). Reconstructed CO₂ concentration data for much of the Miocene are quite sparse if we exclude the MCO and the MCT intervals (Figure 3). Interestingly, when considering boron-based CO₂ reconstructions (e.g., Sossdian et al., 2018), both the CE2 cooling (~ 16 Ma) and the CE8 event (~ 13.8 Ma) occurred at CO₂ values of ~ 400 – 500 ppm (Figure 3). Instead, other proxies, reconstruct lower CO₂ concentrations for all CEs after the MCO (Figure 3). It appears that CO₂ values of ~ 400 ppm (or lower) may have been able to shift the relatively warm Miocene climate to a temporarily colder mode.

4.4. Comparison With Other North Atlantic SST Records

Few biomarkers-based SST reconstructions are available for the middle Miocene in the North Atlantic. Existing records are from ODP Site 982 (Rockall Plateau, 57°30.992'N, 15°52.001' W, 1,135 m, Super et al., 2018; calculated paleolatitude ~54°N at 15 Ma, van Hinsbergen et al., 2015), DSDP Site 608 (Azores, 42°50.205'N, 23°05.252' W, 3,526 m, Super et al., 2018, 2020, calculated paleolatitude ~39°N at 15 Ma, van Hinsbergen et al., 2015). SSTs in these records were calculated using the Bayesian calibration (BAYSPAR) (Tierney & Tingley, 2014, 2015). For a direct comparison, we also recalibrated our data from Site U1318 using BAYSPAR (Figure 3 and Supplemental Data set 1). As reported before, values obtained with BAYSPAR do not differ much with the calibration of Kim et al. (2010) shown in Figure 2 (Supplemental Data set 1).

Although significant differences in resolution exist among the records, some SST patterns can be recognized. In the MCO interval (16.6–14.5 Ma), SST at Site 608 is much higher (average ~30°C) than that of the other two more northerly sites. Counterintuitively, however, SSTs at Site U1318 are 2°C–3°C lower between 16.3 and 15.5 Ma than those of the northern Site 982. Between 14.4 and 13.9 Ma, the three sites show comparable temperatures. More interesting is the SST record between 13.8 and 12.6 Ma. There is a remarkable similarity in SST trends between the Azores Site 608 and Site U1318, while temperatures at Site 982 do not show major changes. Future research should focus on increasing the resolution of the Rockall Plateau record to detect the influence of the (proto)NAC at this site. If higher resolution SST data confirm no major changes in SST also during global CEs, tectonic changes occurred around 14 Ma (Bialik et al., 2019; Hamon et al., 2013; Jakobsson et al., 2007; Montes et al., 2015; Zhang et al., 2014) may have been responsible for the regional variability recorded in the North Atlantic, superimposed on global drivers of climate change. The 2°C–3°C SST difference between Sites 608 and U1318 records, especially during the warmer phases, is similar to the present-day SST difference at the two sites (mean annual SST at Site 608 = 16.6°C and mean annual SST at Site U1318 = 12.6°C).

5. Conclusions

We presented the first high-resolution multiproxy middle Miocene SST and SSP record from a shelf site (Site U1318) in the Porcupine Basin, in the eastern North Atlantic. Warm (average SST_{TEX-H} = ~24°C) and mostly stratified waters are reconstructed for the MCO, ~12°C higher than at present, which cooled by ~3°C (average SST_{TEX-H} = ~21°C) across the MCT. Proxies show transient and long-term coolings, some of which correspond to global increases in benthic $\delta^{18}\text{O}$ including Mi-2, Mi-3, and Mi-4 events. Most of the CEs at Site U1318 are associated with intervals of high surface water productivity. Dinocyst proxies record a ~200 kyr-long period (~13.8–13.6 Ma) with primary productivity significantly higher than that recorded in the modern system (SSP_{DINO} 0.2–0.3 compared to SSP_{DINO} = 0.01). High productivity begins ~100 kyr after a temperature (SST_{DINO}) drop at ~13.9 Ma (CE8). CE8 is synchronous with the global event known as Mi-3 (~13.8 Ma) and coincides with the MCT. The high productivity interval is also synchronous with the global carbon isotope maximum event CM6 (Holbourn et al., 2004) recorded in the deep ocean and indicative of a major perturbation of the carbon cycle. If carbon production in the surface waters of shelf areas led to carbon burial globally, shelves indeed represent the locations where an important feedback mechanism contributing to long-term atmospheric CO₂ decline occurs, as recently suggested by Sosdian et al. (2020). This aspect merits scientific attention and more records from shelf areas can provide the answer.

We compared the surface temperature records of three North Atlantic sites and detected concurrent cooling at ~13.8 Ma in the Azores and Porcupine Basin sites. The record of Site 982 does not seem to show any major cooling at ~13.8 Ma, but the temporal resolution is too low to draw conclusions.

High-resolution temporal records, similar to those produced for the Late Miocene (Herbert et al., 2016), are needed to understand the link between tectonic, global climate, and oceanography changes in different locations of the North Atlantic during the MCT. Interestingly, tectonic changes in seaways, including the complete opening and deepening of the Arctic gateway (Fram Strait, Jakobsson et al., 2007), changes in the Tethys Seaways and in the Mediterranean outflow (Bialik et al., 2019; Hamon et al., 2013; Zhang et al., 2014), and possibly the complete closure of the Central Atlantic Seaway (Montes et al., 2015) occurred around 14 Ma.

Conflict of Interest

The authors declare no conflicts of interest relevant to this study.

Data Availability Statement

All data can be found in the Supplementary Data sets 1 and 2. Data are available at the PANGAEA website (<http://doi.org/10.1594/PANGAEA.926326>).

Acknowledgments

The samples for this study were provided by the Integrated Ocean Discovery Program. Walter Hale and Alex Wülbbers kindly supported the sampling at the Bremen Core Repository. Ivo Vandemoortel is thanked for helping with isotope analyses. Anhelique Mets, Jort Ossebaar, Monique Verweij (NIOZ), and Sabine Van Cauwenberghe (UGent) are thanked for their technical assistance. We thank James Super and Matt Huber for sharing the biomarker data of ODP Site 982 and Sindia Sosdian for sharing CO₂ data. We thank Stijn de Schepper and one anonymous reviewer for their comments, which greatly improved the manuscript. This work was supported by the Research Foundation-Flanders (FWO) under project number G.0179.11N. SS thanks the Netherlands Earth System Science Center, funded by the Ministry of Education, Culture and Science (OCW).

References

- Badger, M. P. S., Lear, C. H., Pancost, R. D., Foster, G. L., Bailey, T. R., Leng, M. J., & Abels, H. A. (2013). CO₂ drawdown following the middle Miocene expansion of the Antarctic Ice Sheet. *Paleoceanography*, *28*, 42–53. <https://doi.org/10.1002/palo.20015>
- Bale, N. J., Villanueva, L., Hopmans, E. C., Schouten, S., & Sinninghe Damsté, J. S. (2013). Different seasonality of pelagic and benthic Thaumarchaeota in the North Sea. *Biogeosciences*, *10*, 7195–7206. <https://doi.org/10.5194/bg-10-7195-2013>
- Barton, A. D., Lozier, M. S., & Williams, R. G. (2015). Physical controls of variability in North Atlantic phytoplankton communities. *Limnology & Oceanography*, *60*(1), 181–197. <https://doi.org/10.1002/lno.10011>
- Besseling, M., Hopmans, E. C., Koenen, M., van der Meer, M. T. J., Vreugdenhil, S., Schouten, S., et al. (2019). Depth-related differences in archaeal populations impact the isoprenoid tetraether lipid composition of the Mediterranean Sea water column. *Organic Geochemistry*, *135*, 16–31. <https://doi.org/10.1016/j.orggeochem.2019.06.008>
- Bialik, O. M., Frank, M., Betzler, C., Zammit, R., & Waldmann, N. D. (2019). Two-step closure of the Miocene Indian Ocean Gateway to the Mediterranean. *Scientific Reports*, *9*, 8842. <https://doi.org/10.1038/s41598-019-45308-7>
- Bijl, P. K., Houben, A. J. P., Hartman, J. D., Pross, J., Salabarnada, A., Escutia, C., & Sangiorgi, F. (2018). Paleoclimatology and ice sheet variability offshore Wilkes Land, Antarctica—Part 2: Insights from Oligocene–Miocene dinoflagellate cyst assemblages. *Climate of the Past*, *14*, 1015–1033. <https://doi.org/10.5194/cp-14-1015-2018>
- Boessenkool, K. P., Van Gelder, M., Brinkhuis, H., & Troelstra, S. R. (2001). Distribution of organic-walled dinoflagellate cysts in surface sediments from transects across the Polar Front offshore southeast Greenland. *Journal of Quaternary Science*, *16*, 661–666. <https://doi.org/10.1002/jqs.654>
- Böhme, M. (2003). The Miocene Climatic Optimum: Evidence from ectothermic vertebrates of Central Europe. *Palaeogeography, Palaeoclimatology, Palaeoecology*, *195*, 389–401. [https://doi.org/10.1016/S0031-0182\(03\)00367-5](https://doi.org/10.1016/S0031-0182(03)00367-5)
- Boyer, T. P., Baranova, O. K., Coleman, C., Garcia, H. E., Grodsky, A., Locarnini, R. A., et al. (2018). World ocean database 2018. In A. V. Mishonov (Ed.), (Tech. Ed.), NOAA Atlas NESDIS 87.
- Brennan, I. J., & Keogh, J. S. (2018). Miocene biome turnover drove conservative body size evolution across Australian vertebrates. *Proceedings of the Royal Society B: Biological Sciences*, *285*, 20181474. <https://doi.org/10.1098/rspb.2018.1474>
- Coste, B., Le Corre, P., & Minas, H. J. (1988). Re-evaluation of the nutrient exchanges in the Strait of Gibraltar. *Deep-Sea Research, Part A*, *35*, 767–775. [https://doi.org/10.1016/0198-0149\(88\)90029-5](https://doi.org/10.1016/0198-0149(88)90029-5)
- Crampton, J. S., Cody, R. D., Levy, R., Harwood, D., McKay, R., & Naish, T. R. (2016). Southern Ocean phytoplankton turnover in response to stepwise Antarctic cooling over the past 15 million years. *Proceedings of the National Academy of Sciences of the United States of America*, *113*, 6868–6873. <https://doi.org/10.1073/pnas.1600318113>
- Dale, B. (1996). Dinoflagellate cyst ecology: Modeling and geological applications. In J. Jansoni & D. C. McGregor (Eds.), *Palynology: Principles and applications* (Vol. 3, pp. 1249–1275). Salt Lake City, UT: American Association of Stratigraphic Palynologists Foundation.
- De Leeuw, J. W., van der Meer, F. W., Rijpstra, W. I. C., & Schenck, P. A. (1980). On occurrence and structural identification of long chain unsaturated ketones and hydrocarbons in sediments. In A. G. Douglas & J. R. Maxwell (Eds.), *Advances in organic geochemistry* (pp. 211–217). Oxford: Pergamon Press. [https://doi.org/10.1016/0079-1946\(79\)90105-8](https://doi.org/10.1016/0079-1946(79)90105-8)
- De Schepper, S., Fischer, E. I., Groeneveld, J., Head, M. J., & Matthiessen, J. (2011). Deciphering the palaeoecology of Late Pliocene and Early Pleistocene dinoflagellate cysts. *Palaeogeography, Palaeoclimatology, Palaeoecology*, *309*, 17–32. <https://doi.org/10.1016/j.palaeo.2011.04.020>
- De Schepper, S., Groeneveld, J., Naafs, B. D. A., Van Renterghem, C., Hennissen, J., Head, M. J., et al. (2013). Northern Hemisphere glaciation during the globally warm Early Late Pliocene. *PLoS One*, *8*(12), e81508. <https://doi.org/10.1371/journal.pone.0081508>
- De Schepper, S., Head, M. J., & Groeneveld, J. (2009). North Atlantic Current variability through marine isotope stage M2 (circa 3.3 Ma) during the mid-Pliocene. *Paleoceanography*, *24*, PA4206. <https://doi.org/10.1029/2008PA001725>
- De Vernal, A., & Marret, F. (2007). Organic-walled dinoflagellate cysts: Tracers of sea-surface conditions. *Developments in Marine Geology*, *1*, 371–408. [https://doi.org/10.1016/S1572-5480\(07\)01014-7](https://doi.org/10.1016/S1572-5480(07)01014-7)
- De Vleeschouwer, D., Vahlenkamp, M., Crucifix, M., & Pälike, H. (2017). Alternating Southern and Northern Hemisphere climate response to astronomical forcing during the past 35 m.y. *Geology*, *45*(4), 375–378. <https://doi.org/10.1130/G38663.1>
- Diester-Haass, L., Billups, K., Gröcke, D. R., Francois, L., Lefebvre, V., & Emeis, K. C. (2009). Mid-Miocene paleoproductivity in the Atlantic Ocean and implications for the global carbon cycle. *Paleoceanography*, *24*, PA1209. <https://doi.org/10.1029/2008PA001605>
- Donders, T. H., Weijers, J. W. H., Munsterman, D. K., Kloosterboer-van Hoeve, M. L., Buckles, L. K., Pancost, R. D., et al. (2009). Strong climate coupling of terrestrial and marine environments in the Miocene of northwest Europe. *Earth and Planetary Science Letters*, *281*, 215–225. <https://doi.org/10.1016/j.epsl.2009.02.034>
- Eronen, J. T., Fortelius, M., Micheels, A., Portmann, F. T., Puolamäki, K., & Janis, C. M. (2012). Neogene aridification of the Northern Hemisphere. *Geology*, *40*(9), 823–826. <https://doi.org/10.1130/G33147.1>
- Expedition 307 Scientists. (2006). Site U1318. In T. G. Ferdelman, A. Kano, T. Williams, J.-P. Henriot, & The Expedition 307 Scientists (Eds.), *Proceedings of the Integrated Ocean Drilling Program* (Vol. 307, pp. 1–57). Washington, DC: Integrated Ocean Drilling Program Management International.
- Faye, S., Rochon, A., & St-Onge, G. (2018). Distribution of modern dinoflagellate cyst assemblages in surface sediments of San Jorge Gulf (Patagonia, Argentina). *Oceanography*, *31*, 122–131. <https://doi.org/10.5670/oceanog.2018.416>
- Flower, B. P., & Kennett, J. P. (1993). Middle Miocene ocean-climate transition: High-resolution oxygen and carbon isotopic records from Deep Sea Drilling Project Site 588A, southwest Pacific. *Paleoceanography*, *8*(6), 811–843. <https://doi.org/10.1029/93PA02196>

- Flower, B. P., & Kennett, J. P. (1994). The middle Miocene climatic transition: East Antarctic ice sheet development, deep ocean circulation and global carbon cycling. *Palaeogeography, Palaeoclimatology, Palaeoecology*, *108*, 537–555. [https://doi.org/10.1016/0031-0182\(94\)90251-8](https://doi.org/10.1016/0031-0182(94)90251-8)
- Foster, G. L., Lear, C. H., & Rae, J. W. B. (2012). The evolution of pCO₂, ice volume and climate during the middle Miocene. *Earth and Planetary Science Letters*, *341–344*, 243–254. <https://doi.org/10.1016/j.epsl.2012.06.007>
- Fujii, R., & Matsuoka, K. (2005). Seasonal change of dinoflagellates cyst flux collected in a sediment trap in Omura Bay, West Japan. *Journal of Plankton Research*, *28*(2), 131–147. <https://doi.org/10.1093/plankt/fbi106>
- García-Ibáñez, M. I., Pardo, P. C., Carracedo, L. I., Mercier, H., Lherminier, P., Rios, A., & Pérez, F. (2015). Structure, transports and transformations of the water masses in the Atlantic Subpolar Gyre. *Progress in Oceanography*, *135*, 18–36. <https://doi.org/10.1016/j.pocean.2015.03.009>
- Gasson, E., DeConto, R. M., Pollard, D., & Levy, R. H. (2016). Dynamic Antarctic ice sheet during the early to mid-Miocene. *Proceedings of the National Academy of Sciences of the United States of America*, *113*(13), 3459–3464. <https://doi.org/10.1073/pnas.1516130113>
- Gibbard, P. L., & Lewin, J. (2003). The history of the major rivers of southern Britain during the Tertiary. *Journal of the Geological Society London*, *160*, 829–845.
- Goldner, A., Herold, N., & Huber, M. (2014). The challenge of simulating the warmth of the mid-Miocene Climatic Optimum in CESM1. *Climate of the Past*, *10*, 523–536. <https://doi.org/10.5194/cp-10-523-2014>
- Greenop, R., Foster, G. L., Wilson, P. A., & Lear, C. H. (2014). Middle Miocene climate instability associated with high-amplitude CO₂ variability. *Paleoceanography*, *29*, 845–853. <https://doi.org/10.1002/2014PA002653>
- Gutknecht, E., Reffray, G., Mignot, A., Dabrowski, T., & Sotillo, M. G. (2019). Modeling the marine ecosystem of Iberia–Biscay–Ireland (IBI) European waters for CMEMS operational applications. *Ocean Science*, *15*, 1489–1516. <https://doi.org/10.5194/os-15-1489-2019>
- Hamon, N., Sepulchre, P., Lefebvre, V., & Ramstein, G. (2013). The role of eastern Tethys Seaway closure in the middle Miocene climatic transition (ca. 14 Ma). *Climate of the Past*, *9*(6), 2687–2702. <https://doi.org/10.5194/cp-9-2687-2013>
- Head, M. J. (1996). Modern dinoflagellate cysts and their biological affinities. In J. Jansoni & D. C. McGregor (Eds.), *Palynology: Principles and applications* (Vol. 3, pp. 1197–1248). Salt Lake City, UT: American Association of Stratigraphic Palynologists Foundation.
- Hennissen, J. A. I., Head, M. J., De Schepper, S., & Groeneveld, J. (2014). Palynological evidence for a southward shift of the North Atlantic Current at ~2.6 Ma during the intensification of late Cenozoic Northern Hemisphere glaciation. *Paleoceanography*, *29*, 564–580. <https://doi.org/10.1002/2013PA002543>
- Herbert, T., Lawrence, K., Tzanova, A., Peterson, L., Caballero-Gill, R., & Kelly, C. (2016). Late Miocene global cooling and the rise of modern ecosystems. *Nature Geoscience*, *9*, 843–847. <https://doi.org/10.1038/ngeo2813>
- Herold, N., Huber, M., Müller, R. D., & Seton, M. (2012). Modeling the Miocene Climatic Optimum: Ocean circulation. *Paleoceanography*, *27*, PA1209. <https://doi.org/10.1029/2010PA002041>
- Heslop, D., De Schepper, S., & Proske, U. (2011). Diagnosing the uncertainty of taxa relative abundances derived from count data. *Marine Micropaleontology*, *79*(3–4), 114–120.
- Ho, S., & Laepple, T. (2016). Flat meridional temperature gradient in the early Eocene in the subsurface rather than surface ocean. *Nature Geoscience*, *9*, 606–610.
- Holbourn, A., Kuhnt, W., Kochhann, K. G. D., Andersen, N., & Meier, K. J. S. (2015). Global perturbation of the carbon cycle at the onset of the Miocene Climatic Optimum. *Geology*, *43*, 123–126. <https://doi.org/10.1130/G36317.1>
- Holbourn, A., Kuhnt, W., Lyle, M. W., Schneider, L., Romero, O. E., & Andersen, N. (2014). Middle Miocene climate cooling linked to intensification of eastern equatorial Pacific upwelling. *Geology*, *42*(1), 19–22. <https://doi.org/10.1130/G34890.1>
- Holbourn, A., Kuhnt, W., Schulz, M., & Erlenkeuser, H. (2005). Impacts of orbital forcing and atmospheric CO₂ on Miocene ice-sheet expansion. *Nature*, *438*, 483–487. <https://doi.org/10.1038/nature04123>
- Holbourn, A., Kuhnt, W., Schulz, M., Flores, J., & Andersen, N. (2007). Orbitally-paced climate evolution during the middle Miocene “Monterey” carbon-isotope excursion. *Earth and Planetary Science Letters*, *261*, 534–550. <https://doi.org/10.1016/j.epsl.2007.07.026>
- Holbourn, A., Kuhnt, W., Simo, J. A., & Li, Q. Y. (2004). Middle Miocene isotope stratigraphy and paleoceanographic evolution of the northwest and southwest Australian margins (Wombat Plateau and Great Australian Bight). *Palaeogeography, Palaeoclimatology, Palaeoecology*, *208*, 1–22. <https://doi.org/10.1016/j.palaeo.2004.02.003>
- Hopmans, E. C., Weijers, J. W. H., Schefuß, E., Herfort, L., Sinnighe Damsté, J. S., & Schouten, S. (2004). A novel proxy for terrestrial organic matter in sediments based on branched and isoprenoid tetraether lipids. *Earth and Planetary Science Letters*, *224*, 107–116. <https://doi.org/10.1016/j.epsl.2004.05.012>
- Huertas, I. E., Rios, A. F., García-Lafuente, J., Navarro, G., Makaoui, A., Sánchez-Román, A., et al. (2012). Atlantic forcing of the Mediterranean oligotrophy. *Global Biogeochemical Cycles*, *26*, GB2022. <https://doi.org/10.1029/2011GB004167>
- Hurley, S. J., Elling, F. J., Könneke, M., Buchwald, C., Wankel, S. D., Santoro, A. E., et al. (2016). Influence of ammonia oxidation rate on Thaumarchaeal lipid composition and the TEX₈₆ temperature proxy. *Proceedings of the National Academy of Sciences of the United States of America*, *113*(28), 7762–7767. <https://doi.org/10.1073/pnas.1518534113>
- IPCC. (2014). Climate change 2014: Synthesis report. In Core Writing Team, R. K. Pachauri, & L. A. Meyer (Eds.), *Contribution of Working Groups I, II and III to the Fifth Assessment Report of the Intergovernmental Panel on Climate Change*. (151 pp.). Geneva, Switzerland: IPCC.
- Jacobson, D., & Anderson, D. (2008). Thecate heterotrophic dinoflagellates: Feeding behavior and mechanisms. *Journal of Phycology*, *22*, 249–258. <https://doi.org/10.1111/j.1529-8817.1986.tb00021.x>
- Jakobsson, M., Backman, J., Rudels, B., Nycander, J., Frank, M., Mayer, L., et al. (2007). The Early Miocene onset of a ventilated circulation regime in the Arctic Ocean. *Nature*, *447*, 986–990. <https://doi.org/10.1038/nature05924>
- John, C. M., Karner, G. D., Browning, E., Leckie, R. M., Mateo, Z., Carson, B., & Lowery, C. (2011). Timing and magnitude of Miocene eustasy derived from the mixed siliciclastic-carbonate stratigraphic record of the northeastern Australian margin. *Earth and Planetary Science Letters*, *304*, 455–467. <https://doi.org/10.1016/j.epsl.2011.02.013>
- Kasbohm, J., & Schoene, B. (2018). Rapid eruption of the Columbia River flood basalt and correlation with the mid-Miocene climate optimum. *Science Advances*, *4*(9), eaat8223. <https://doi.org/10.1126/sciadv.aat8223>
- Kender, S., Peck, V. L., Jones, R. W., & Kaminski, M. A. (2009). Middle Miocene oxygen minimum zone expansion offshore West Africa: Evidence for global cooling precursor events. *Geology*, *37*, 699–702. <https://doi.org/10.1130/G30070A.1>
- Kim, J.-H., Crosta, X., Michel, E., Schouten, S., Duprat, J., & Sinnighe Damsté, J. S. (2009). Impact of lateral transport on organic proxies in the Southern Ocean. *Quaternary Research*, *71*, 246–250. <https://doi.org/10.1016/j.yqres.2008.10.005>
- Kim, J.-H., van der Meer, J., Schouten, S., Helmke, P., Willmott, V., Sangiorgi, F., et al. (2010). New indices and calibrations derived from the distribution of crenarchaeal isoprenoid tetraether lipids: Implications for past sea surface temperature reconstructions. *Geochimica et Cosmochimica Acta*, *74*, 4639–4654. <https://doi.org/10.1016/j.gca.2010.05.027>

- Kürschner, W. M., Kvacek, Z., & Dilcher, D. L. (2008). The impact of Miocene atmospheric carbon dioxide fluctuations on climate and the evolution of terrestrial ecosystems. *Proceedings of the National Academy of Sciences of the United States of America*, *105*, 449–453. <https://doi.org/10.1073/pnas.0708588105>
- Lawrence, K. T., Pearson, A., Castañeda, I. S., Ladlow, C., Peterson, L. C., & Lawrence, C. E. (2020). Comparison of late Neogene Uk'37 and TEX86 paleotemperature records from the eastern equatorial Pacific at orbital resolution. *Paleoceanography and Paleoclimatology*, *35*, e2020PA003858. <https://doi.org/10.1029/2020PA003858>
- Lear, C. H., Coxall, H. K., Foster, G. L., Lunt, D. J., Mawbey, E. M., Rosenthal, Y., et al. (2015). Neogene ice volume and ocean temperatures: Insights from infaunal foraminiferal Mg/Ca paleothermometry. *Paleoceanography*, *30*, 1437–1454. <https://doi.org/10.1002/2015PA002833>
- Lear, C. H., Mawbey, E. M., & Rosenthal, Y. (2010). Cenozoic benthic foraminiferal Mg/Ca and Li/Ca records: Toward unlocking temperatures and saturation states. *Paleoceanography*, *25*, PA4215. <https://doi.org/10.1029/2009PA001880>
- Lengger, S. K., Kraaij, M., Tjallingii, R., Baas, M., Stuut, J.-B., Hopmans, E. C., et al. (2013). Differential degradation of intact polar and core glycerol dialkyl glycerol tetraether lipids upon post-depositional oxidation. *Organic Geochemistry*, *65*, 83–93. <https://doi.org/10.1016/j.orggeochem.2013.10.004>
- Levy, R. H., Harwood, D., Florindo, F., Sangiorgi, F., Tripathi, R., von Eynatten, H., et al. (2016). Antarctic ice sheet sensitivity to atmospheric CO₂ variations in the early to mid-Miocene. *Proceedings of the National Academy of Sciences of the United States of America*, *113*(13), 3453–3458. <https://doi.org/10.1073/pnas.1516030113>
- Levy, R. H., Meyers, S. R., Naish, T. R., Golledge, N. R., McKay, R. M., Crampton, J. S., et al. (2019). Antarctic ice-sheet sensitivity to obliquity forcing enhanced through ocean connections. *Nature Geoscience*, *12*, 132–137. <https://doi.org/10.1038/s41561-018-0284-4>
- Lewis, J., Dodge, J. D., & Powell, A. J. (1990). Quaternary dinoflagellate cysts from the upwelling system offshore Peru, Hole 686B, ODP LEG 112. *Proceedings of the Ocean Drilling Program, Scientific Results*, *112*, 323–327.
- Limoges, A., De Vernal, A., & Van Nieuwenhove, N. (2014). Long-term hydrological changes in the northeastern Gulf of Mexico (ODP-625B) during the Holocene and late Pleistocene inferred from organic-walled dinoflagellate cysts. *Palaeogeography, Palaeoclimatology, Palaeoecology*, *414*, 178–191. <https://doi.org/10.1016/j.palaeo.2014.08.019>
- Lozier, M. S., Li, F., Bacon, S., Bahr, F., Bower, A. S., Cunningham, et al. (2019). A sea change in our view of overturning in the subpolar North Atlantic. *Science*, *363*, 516–221. <https://doi.org/10.1126/science.aau6592>
- Mangelsdorf, K., Zink, K.-G., di Primio, R., & Horsfield, B. (2011). Microbial lipid markers within and adjacent to Challenger Mound in the Belgica carbonate mound province, Porcupine Basin, offshore Ireland (IODP Expedition 307). *Marine Geology*, *282*(1–2), 91–101. <https://doi.org/10.1016/j.margeo.2010.05.007>
- Miller, K. G., Browning, J. V., Schmelz, W. J., Kopp, R. E., Mountain, G. S., & Wright, J. D. (2020). Cenozoic sea-level and cryospheric evolution from deep-sea geochemical and continental margin records. *Science Advances*, *6*, eaaz1346. <https://doi.org/10.1126/sciadv.aaz1346>
- Miller, K. G., Wright, J. D., & Fairbanks, R. G. (1991). Unlocking the Ice House: Oligocene–Miocene oxygen isotopes, eustasy, and margin erosion. *Journal of Geophysical Research*, *96*(B4), 6829–6848. <https://doi.org/10.1029/90JB02015>
- Mollenhauer, G., Eglinton, T. I., Hopmans, E. C., & Sinninghe Damsté, J. S. (2008). A radiocarbon-based assessment of the preservation characteristics of crenarchaeol and alkenones from continental margin sediments. *Organic Geochemistry*, *39*(8), 1039–1045. <https://doi.org/10.1016/j.orggeochem.2008.02.006>
- Montes, C., Cardona, A., Jaramillo, C., Pardo, A., Silva, J. C., Valencia, V., et al. (2015). Middle Miocene closure of the Central American Seaway. *Science*, *348*(6231), 226–229. <https://doi.org/10.1126/science.aaa2815>
- Müller, O., Wilson, B., Paulsen, M. L., Runińska, A., Armo, H. R., Bratak, G., & Øvreås, L. (2018). Spatiotemporal dynamics of ammonia-oxidizing Thaumarchaeota in distinct Arctic water masses. *Frontiers in Microbiology*, *9*, 24. <https://doi.org/10.3389/fmicb.2018.00024>
- Müller, P. J., Kirst, G., Ruhland, G., von Storch, I., & Rosell-Melé, A. (1998). Calibration of the alkenone paleotemperature index U₃₇^{Kr} based on core-tops from the eastern South Atlantic and the global ocean (60°N–60°S). *Geochimica et Cosmochimica Acta*, *62*(10), 1757–1772. [https://doi.org/10.1016/S0016-7037\(98\)00097-0](https://doi.org/10.1016/S0016-7037(98)00097-0)
- Pitcher, A., Villanueva, L., Hopmans, E. C., Schouten, S., Reichart, G. J., & Sinninghe Damsté, J. S. (2011). Niche segregation of ammonia-oxidizing archaea and anammox bacteria in the Arabian Sea oxygen minimum zone. *The ISME Journal*, *5*(12), 1896–1904. <https://doi.org/10.1038/ismej.2011.60>
- Pollard, R. T., Griffiths, M. J., Cunningham, S., Read, J. F., Pérez, F. F., & Ríos, A. F. (1996). Vivaldi 1991: A study of the formation, circulation and ventilation of eastern North Atlantic Central Water. *Progress in Oceanography*, *37*, 167–172. [https://doi.org/10.1016/S0079-6611\(96\)00008-0](https://doi.org/10.1016/S0079-6611(96)00008-0)
- Pospelova, V., De Vernal, A., & Pedersen, T. F. (2008). Distribution of dinoflagellate cysts in surface sediments from the northeastern Pacific Ocean (43–25°N) in relation to sea-surface temperature, productivity and coastal upwelling. *Marine Micropaleontology*, *68*(1–2), 21–48. <https://doi.org/10.1016/j.marmicro.2008.01.008>
- Pospelova, V., Zonneveld, K. A. F., Heikkilä, M., Bringué, M., Price, A., Esenkulova, S., & Matsuoka, K. (2018). Seasonal, annual, and inter-annual *Spiniferites* cyst production: A review of sediment trap studies. *Palynology*, *42*(S1), 162–181. <https://doi.org/10.1080/01916122.2018.1465738>
- Pound, M. J., Haywood, A. M., Salzmann, U., & Riding, J. B. (2012). Global vegetation dynamics and latitudinal temperature gradients during the Mid to late Miocene (15.97–5.33 Ma). *Earth-Science Reviews*, *112*, 1–22. <https://doi.org/10.1016/j.earscirev.2012.02.005>
- Prahl, F. G., & Wakeham, S. G. (1987). Calibration of unsaturation patterns in long-chain ketone compositions for paleotemperature assessment. *Nature*, *330*(6146), 367–369. <https://doi.org/10.1038/330367a0>
- Prebble, J., Crouch, E., Carter, L., Cortese, G., Bostock, H., & Neil, H. (2013). An expanded modern dinoflagellate cyst dataset for the Southwest Pacific and Southern Hemisphere with environmental associations. *Marine Micropaleontology*, *101*, 33–48. <https://doi.org/10.1016/j.marmicro.2013.04.004>
- Pross, J., & Brinkhuis, H. (2005). Organic-walled dinoflagellate cysts as paleoenvironmental indicators in the Paleogene; a synopsis of concepts. *Paläontologische Zeitschrift*, *79*(1), 53–59. <https://doi.org/10.1007/BF03021753>
- Quaijtaal, W., Donders, T. H., Persico, D., & Louwe, S. (2014). Characterising the middle Miocene Mi-events in the Eastern North Atlantic realm: A first high-resolution marine palynological record from the Porcupine Basin. *Palaeogeography, Palaeoclimatology, Palaeoecology*, *399*, 140–159. <https://doi.org/10.1016/j.palaeo.2014.02.017>
- Quaijtaal, W., Tesseur, S., Donders, T. H., Claeys, P., & Louwe, S. (2017). A revised and improved age model for the middle Miocene part of IODP Site U1318 (Porcupine Basin, offshore southwestern Ireland). *Geological Magazine*, *155*(5), 1105–1116. <https://doi.org/10.1017/S0016756816001278>
- Raddatz, J., Rüggeberg, A., Margreth, S., & Dullo, W.-C.; the IODP Expedition 307 Scientific Party. (2011). Paleoenvironmental reconstruction of challenger mound initiation in the Porcupine Seabight, NE Atlantic. *Marine Geology*, *282*, 79–90. <https://doi.org/10.1016/j.margeo.2010.10.019>

- Raymo, M. E. (1991). Geochemical evidence supporting T.C. Chamberlin's theory of glaciation. *Geology*, *19*, 344–347. [https://doi.org/10.1306/0091-7613\(1991\)019<0344:GESTCC>2.3.CO;2](https://doi.org/10.1306/0091-7613(1991)019<0344:GESTCC>2.3.CO;2)
- Reichart, G.-J., & Brinkhuis, H. (2003). Late Quaternary *Protoperidinium* cysts as indicators of paleoproductivity in the northern Arabian Sea. *Marine Micropaleontology*, *49*, 303–370. [https://doi.org/10.1016/S0377-8398\(03\)00050-1](https://doi.org/10.1016/S0377-8398(03)00050-1)
- Retallack, G. J. (2009). Refining a pedogenic-carbonate CO₂ paleobarometer to quantify a middle Miocene greenhouse spike. *Palaeoogeography, Palaoclimatology, Palaeoecology*, *281*, 57–65. <https://doi.org/10.1016/j.palaeo.2009.07.011>
- Ribeiro, S., & Amorim, A. (2008). Environmental drivers of temporal succession in recent dinoflagellate cyst assemblages from a coastal site in the North-East Atlantic (Lisbon Bay, Portugal). *Marine Micropaleontology*, *68*, 156–178.
- Rice, A. L., Billett, D. S. M., Thurston, M. H., & Lampitt, R. S. (1991). The Institute of Oceanographic Sciences Biology programme in the Porcupine Seabight: Background and general introduction. *Journal of the Marine Biological Association of the United Kingdom*, *71*, 281–310. <https://doi.org/10.1017/S0025315400051614>
- Rosell-Melé, A., Eglinton, G., Pflaumann, U., & Sarnthein, M. (1995). Atlantic core-top calibration of the U₃₇^K index as a sea-surface palaeotemperature indicator. *Geochimica et Cosmochimica Acta*, *59*(15), 3099–3107. [https://doi.org/10.1016/0016-7037\(95\)00199-A](https://doi.org/10.1016/0016-7037(95)00199-A)
- Ryan, M. C., Helland-Hansen, W., Johannessen, E. P., & Steel, R. J. (2009). Erosional vs. accretionary shelf margins: The influence of margin type on deepwater sedimentation: An example from the Porcupine Basin, offshore western Ireland. *Basin Research*, *21*, 676–703. <https://doi.org/10.1111/j.1365-2117.2009.00424.x>
- Sangiorgi, F., Bijl, P. K., Passchier, S., Salzmann, U., Schouten, S., McKay, R., et al. (2018). Southern Ocean warming and Wilkes Land ice sheet retreat during the mid-Miocene. *Nature Communications*, *9*, 317. <https://doi.org/10.1038/s41467-017-02609-7>
- Sangiorgi, F., Brumsack, H.-J., Willard, D. A., Schouten, S., Stickley, C. E., O'Regan, M., et al. (2008). A 26 million years gap in the central Arctic record at the Greenhouse–Icehouse transition: Looking for clues. *Paleoceanography*, *23*, PA1S04. <https://doi.org/10.1029/2007PA001477>
- Sangiorgi, F., Capotondi, L., Combourieu Nebout, N., Vigliotti, L., Brinkhuis, H., Giunta, S., et al. (2003). Holocene seasonal sea surface temperature variations in the South Adriatic Sea inferred from a multi-proxy approach. *Journal of Quaternary Science*, *18*, 723–732. <https://doi.org/10.1002/jqs.782>
- Sangiorgi, F., & Donders, T. H. (2004). Reconstructing 150 years of eutrophication in the north-western Adriatic Sea (Italy) using dinoflagellate cysts, pollen and spores. *Estuarine, Coastal and Shelf Science*, *60*(1), 69–79. <https://doi.org/10.1016/j.ecss.2003.12.001>
- Schouten, S., Woltering, M., Rijpstra, W. I. C., Sluijs, A., Brinkhuis, H., & Sinninghe Damsté, J. S. (2007). The Paleocene–Eocene carbon isotope excursion in higher plant organic matter: Differential fractionation of angiosperms and conifers in the Arctic. *Earth and Planetary Science Letters*, *258*, 581–592. <https://doi.org/10.1016/j.epsl.2007.04.024>
- Schreck, M., Matthiessen, J., & Head, M. J. (2012). A magnetostratigraphic calibration of middle Miocene through Pliocene dinoflagellate cyst and acritarch events in the Iceland Sea (Ocean Drilling Program Hole 907A). *Review of Palaeobotany and Palynology*, *187*, 66–94. <https://doi.org/10.1016/j.revpalbo.2012.08.006>
- Schreck, M., Méheust, M., Stein, R., & Matthiessen, J. (2013). Response of marine palynomorphs to Neogene climate cooling in the Iceland Sea (ODP Hole 151-907A). *Marine Micropaleontology*, *101*, 49–67. <https://doi.org/10.1016/j.marmicro.2013.03.003>
- Schreck, M., Nam, S.-I., Clotten, C., Fahl, K., De Schepper, S., Forwick, M., & Matthiessen, J. (2017). Neogene dinoflagellate cysts and acritarchs from the high northern latitudes and their relation to sea surface temperature. *Marine Micropaleontology*, *136*, 51–65. <https://doi.org/10.1016/j.marmicro.2017.09.003>
- Scotese, C. R. (2014). *Atlas of Neogene paleogeographic maps (Mollweide projection), Maps 1–7, Volumes 1, the Cenozoic, PALEOMAP atlas for ArcGIS*. Evanston, IL: PALEOMAP Project.
- Shevenell, A. E., Kennett, J. P., & Lea, D. W. (2004). Middle Miocene Southern Ocean cooling and Antarctic cryosphere expansion. *Science*, *305*(5691), 1766–1770. <https://doi.org/10.1126/science.1100061>
- Shevenell, A. E., Kennett, J. P., & Lea, D. W. (2008). Middle Miocene ice sheet dynamics, deep-sea temperatures, and carbon cycling: A Southern Ocean perspective. *Geochemistry, Geophysics, Geosystems*, *9*, Q02006. <https://doi.org/10.1029/2007GC001736>
- Shutler, J. D., Land, P. E., Brown, C. W., Findlay, H. S., Donlon, C. J., Medland, M., et al. (2013). Coccolithophore surface distributions in the North Atlantic and their modulation of the air-sea flux of CO₂ from 10 years of satellite Earth observation data. *Biogeosciences*, *10*(4), 2699–2709. <https://doi.org/10.5194/bg-10-2699-2013>
- Sluijs, A., Pross, J., & Brinkhuis, H. (2005). From greenhouse to icehouse; organic walled dinoflagellate cysts as paleoenvironmental indicators in the Paleogene. *Earth-Science Reviews*, *68*, 281–315. <https://doi.org/10.1016/j.earscirev.2004.06.001>
- Sosdian, S. M., Babila, T. L., Greenop, R., Foster, G. L., & Lear, C. H. (2020). Ocean carbon storage across the middle Miocene: A new interpretation for the Monterey Event. *Nature Communications*, *11*(1), 1–11. <https://doi.org/10.1038/s41467-019-13792-0>
- Sosdian, S. M., Greenop, R., Hain, M. P., Foster, G. L., Pearson, P. N., & Lear, C. H. (2018). Constraining the evolution of Neogene ocean carbonate chemistry using the boron isotope pH proxy. *Earth and Planetary Science Letters*, *498*, 362–376. <https://doi.org/10.1016/j.epsl.2018.06.017>
- Steinthsordottir, M., Coxall, H. K., De Boer, A. M., Huber, M., Barbolini, N., Bradshaw, C. D., et al. (2021). The Miocene: The future of the Past. *Paleoceanography and Paleoclimatology*, *36*, e2020PA004037. <https://doi.org/10.1029/2020PA004037>
- Steinthsordottir, M., Jardine, P. E., & Rember, W. B. (2021). Near-future pCO₂ during the hot Miocene Climatic Optimum. *Paleoceanography and Paleoclimatology*, *36*, e2020PA003900. <https://doi.org/10.1029/2020PA003900>
- Stuecker, M. F., Bitz, C. M., Armour, K. C., Proistosescu, C., Kang, S. M., Xie, S.-P., et al. (2018). Polar amplification dominated by local forcing and feedbacks. *Nature Climate Change*, *8*, 1076–1081. <https://doi.org/10.1038/s41558-018-0339-y>
- Super, J. R., Thomas, E., Pagani, M., Huber, M., O'Brien, C., & Hull, P. M. (2018). North Atlantic temperature and pCO₂ coupling in the early-middle Miocene. *Geology*, *46*(6), 519–522. <https://doi.org/10.1130/G40228.1>
- Super, J. R., Thomas, E., Pagani, M., Huber, M., O'Brien, C., & Hull, P. M. (2020). Miocene evolution of North Atlantic sea surface temperature. *Paleoceanography and Paleoclimatology*, *35*, e2019PA003748. <https://doi.org/10.1029/2019PA003748>
- Taylor, K. W., Huber, M., Hollis, C. J., Hernandez-Sanchez, M. T., & Pancost, R. D. (2013). Re-evaluating modern and Palaeogene GDGT distributions: Implications for SST reconstructions. *Global and Planetary Change*, *108*, 158–174. <https://doi.org/10.1016/j.gloplacha.2013.06.011>
- Tierney, J. E., & Tingley, M. P. (2014). A Bayesian, spatially-varying calibration model for the TEX₈₆ proxy. *Geochimica et Cosmochimica Acta*, *127*, 83–106. <https://doi.org/10.1016/j.gca.2013.11.026>
- Tierney, J. E., & Tingley, M. P. (2015). A TEX₈₆ surface sediment database and extended Bayesian calibration. *Scientific Data*, *2*, 150029. <https://doi.org/10.1038/sdata.2015.29>
- UNEP LME Report. (2008). *A perspective on changing conditions of the World's regional seas*. In UNEP regional seas reports and studies (Vol. 182, 852 pp.). Nairobi: UNEP.

- Ustup, G., Ahmad, A., Matsuoka, K., Lim, P. T., & Leaw, C. P. (2011). Biology, ecology and bloom dynamics of the toxic marine dinoflagellate *Pyrodinium bahamense*. *Harmful Algae*, *14*, 301–312. <https://doi.org/10.1016/j.hal.2011.10.026>
- Utescher, T., Ashraf, A., Dreist, A., Dybkjaer, K., Mosbrugger, V., Pross, J., & Volker, W. (2012). Variability of Neogene continental climates in Northwest Europe—A detailed study based on microfloras. *Turkish Journal of Earth Sciences*, *21*, 289–314. <https://doi.org/10.3906/yer-1005-3>
- Van Hinsbergen, D. J., De Groot, L. V., Van Schaik, S. J., Spakman, W., Bijl, P. K., Sluijs, A., et al. (2015). A paleolatitude calculator for paleoclimate studies. *PLoS One*, *10*(6), e0126946. <https://doi.org/10.1371/journal.pone.0126946>
- Versteegh, G. J. M. (1994). Recognition of cyclic and non-cyclic environmental changes in the Mediterranean Pliocene: A palynological approach. *Marine Micropaleontology*, *23*, 147–183. [https://doi.org/10.1016/0377-8398\(94\)90005-1](https://doi.org/10.1016/0377-8398(94)90005-1)
- Versteegh, G. J. M., & Zonneveld, K. A. F. (2002). Use of selective degradation to separate preservation from productivity. *Geology*, *30*(7), 615–618. [https://doi.org/10.1130/0091-7613\(2002\)030<0615:UOSDTS>2.0.CO;2](https://doi.org/10.1130/0091-7613(2002)030<0615:UOSDTS>2.0.CO;2)
- Vincent, E., & Berger, W. H. (1985). Carbon dioxide and polar cooling in the Miocene: The Monterey hypothesis. In E. T. Sundquist & W. S. Broecker (Eds.), *The carbon cycle and atmospheric CO₂: Natural variations Archaean to present*, Geophysical Monograph Series (Vol. 32, pp. 455–468). Washington, DC: American Geophysical Union. <https://doi.org/10.1029/GM032p0455>
- Volkman, J. K., Eglinton, G., Corner, E. D. S., & Sargent, J. R. (1980). Novel unsaturated straight-chain C₃₇/C₃₉ methyl and ethyl ketones in marine sediments and a coccolithophore *Emiliania huxleyi*. In A. G. Douglas & J. R. Maxwell (Eds.), *Advances in organic geochemistry* (pp. 219–227). Oxford: Pergamon Press.
- Wall, D., & Dale, B. (1966). “Living fossils” in western Atlantic plankton. *Nature*, *211*(5053), 1025–1026.
- Wan, S., Kürschner, W. M., Clift, P. D., Li, A., & Li, T. (2009). Extreme weathering/erosion during the Miocene Climatic Optimum: Evidence from sediment record in the South China Sea. *Geophysical Research Letters*, *36*, L19706. <https://doi.org/10.1029/2009GL040279>
- Warny, S., Askin, R. A., Hannah, M. J., Mohr, B. A. R., Raine, J. I., Harwood, D. M., et al. (2009). Palynomorphs from a sediment core reveal a sudden remarkably warm Antarctica during the middle Miocene. *Geology*, *37*, 955–958. <https://doi.org/10.1130/G30139A.1>
- Weijers, J. W. H., Schouten, S., Spaargaren, O. C., & Sinninghe Damsté, J. S. (2006). Occurrence and distribution of tetraether membrane lipids in soils: Implications for the use of the TEX₈₆ proxy and the BIT index. *Organic Geochemistry*, *37*, 1680–1693. <https://doi.org/10.1016/j.orggeochem.2006.07.018>
- Williams, G. L., Fensome, R. A., & MacRae, R. A. (2017). *The Lentini and Williams index of fossil dinoflagellates 2017 edition* (contributions series no. 48). Dallas, TX: American Association of Stratigraphic Palynologists.
- Wood, G. D., Gabriel, A. M., & Lawson, J. C. (1996). In J. Jansonius & D. C. McGregor (Eds.), *Palynology: Principles and applications* (Vol. 1, pp. 29–50). Dallas, TX: American Association of Stratigraphic Palynologists Foundation.
- Woodruff, F., & Savin, S. M. (1991). Mid-Miocene isotope stratigraphy in the deep sea: High resolution correlations, paleoclimatic cycles, and sediment preservation. *Paleoceanography*, *6*(6), 755–806. <https://doi.org/10.1029/91PA02561>
- Wright, J. D., Miller, K. G., & Fairbanks, R. G. (1992). Early and middle Miocene stable isotopes: Implications for Deepwater circulation and climate. *Paleoceanography*, *7*(3), 357. <https://doi.org/10.1029/92PA00760>
- You, Y., Huber, M., Müller, R. D., Poulsen, C. J., & Ribbe, J. (2009). Simulation of the middle Miocene climate optimum. *Geophysical Research Letters*, *36*, L04702. <https://doi.org/10.1029/2008GL036571>
- Zachos, J. C., Dickens, G. R., & Zeebe, R. E. (2008). An early Cenozoic perspective on greenhouse warming and carbon-cycle dynamics. *Nature*, *451*, 279–283. <https://doi.org/10.1038/nature06588>
- Zhang, Y. G., Pagani, M., Liu, Z., Bohaty, S. M., & DeConto, R. (2013). A 40-million-year history of atmospheric CO₂. *Philosophical Transactions of the Royal Society A: Mathematical Physical and Engineering Sciences*, *371*, 1–20. <https://doi.org/10.1098/rsta.2013.0096>
- Zhang, Y. G., Pagani, M., & Wang, Z. (2016). Ring Index: A new strategy to evaluate the integrity of TEX₈₆ paleothermometry. *Paleoceanography*, *31*, 220–232. <https://doi.org/10.1002/2015PA002848>
- Zhang, Y. G., Zhang, C. L., Liu, X. L., Li, L., Hinrichs, K. U., & Noakes, J. E. (2011). Methane Index: A tetraether archeal lipid biomarker indicator for detecting the instability of marine gas hydrates. *Earth and Planetary Science Letters*, *307*, 525–534. <https://doi.org/10.1016/j.epsl.2011.05.031>
- Zhang, Z., Ramstein, G., Schuster, M., Li, C., Contoux, C., & Yan, Q. (2014). Aridification of the Sahara Desert caused by Tethys Sea shrinkage during the Late Miocene. *Nature*, *513*, 401–404. <https://doi.org/10.1038/nature13705>
- Zonneveld, K. A. F., Marret, F., Versteegh, G., Bogus, K., Bonnet, S., Bouimetarhan, I., et al. (2013). Atlas of modern dinoflagellate cyst distribution based on 2405 datapoints. *Review of Palaeobotany and Palynology*, *191*, 1–197. <https://doi.org/10.1016/j.revpalbo.2012.08.003>